# Multiplexed Neuromodulatory-Type-Annotated EM-Reconstruction of Larval Zebrafish

Fu-Ning Li[1,6], Jia-Zheng Liu[2,6], Can Shi[1,4,6], Jing-Bin Yuan[2,3,6], Ya-Nan Lv[2,3,6], Jing Liu[2,6], Li-Na Zhang[2,6], Lin-Lin Li[2,6], Li-Jun Shen[2,6], Xi Chen[2,6], Hao Zhai[2,3], Bo-hao Chen[2,3], Yan-Chao Zhang[2,3], Hao-ran Chen[2,3], Hai-Yang Yan[2,3], Sheng Chang[2], Hong-tu Ma[2], Fang-Xu Zhou[2], Tong Xin[2], Xiao-Hui Dong[2], Li-Mei Lin[2], Xing-Hui Zhao[2], Zheng-Huan Fang[1], Jia-Liang Zu[1,4], Rong-Kun Tao[1], Han-Yang Hu[1], Chen-Ying Qian[1], Yan-Song Wang[1,4], Chang-Mei Zhang[1], Pei-Shan Xiang[1], Yong-Xin Yang[1], Xu-Fei Du[1], Hua Han[2,3,*], Jiu-Lin Du[1,4,5,7,*]

[1] Institute of Neuroscience, State Key Laboratory of Brain Cognition and Brain-Inspired Intelligence Technology, Center for Excellence in Brain Science and Intelligence Technology, Chinese Academy of Sciences, 320 Yue-Yang Road, Shanghai 200031, China

[2] State Key Laboratory of Brain Cognition and Brain-Inspired Intelligence Technology, Institute of Automation, Chinese Academy of Sciences, Beijing 100190, China

[3] School of Future Technology, School of Artificial Intelligence, University of Chinese Academy of Sciences, Beijing 101408, China

[4] University of Chinese Academy of Sciences, 19A Yu-Quan Road, Beijing 100049, China

[5] School of Life Science and Technology, ShanghaiTech University, 319 Yue-Yang Road, Shanghai 200031, China

[6] These authors contributed equally to this work

[7] Lead contact

* Correspondence

Dr. Jiu-Lin Du,
Institute of Neuroscience,
Chinese Academy of Sciences,
Shanghai 200031, China
E-mail: forestdu@ion.ac.cn

Dr. Hua Han,
Institute of Automation,
Chinese Academy of Sciences,
Beijing 100190, China
E-mail: hua.han@ia.ac.cn

## Abstract

The brain is complementarily assembled by the sensorimotor and neuromodulatory (NM) pathways. Mapping the neural connectome is essential for elucidating the synaptic organization principles of this bi-pathway architecture. However, most electron microscopy (EM) reconstructions provide limited information about cell types, in particular NM neurons. Here we present a synapse-level, multiplexed molecular annotated reconstruction of an intact larval zebrafish brain, comprising over 170 thousand cells and 25 million synapses. Noradrenergic, dopaminergic, serotonergic, hypocretinergic/orexinergic, and glycinergic neurons were identified using subcellular localization of APEX2, while glutamatergic and GABAergic neurons were inferred from the Zebrafish Mesoscopic Atlas. NM neurons with varying indegree scale-distinctly innervate various sensory – motor brain regions, exhibiting heterogeneity in synapse number and strength. As a critical NM system, individual locus coeruleus noradrenergic (LC-NE) neurons integrate extensive brain-wide inputs displaying modality-specific spatial organization. Motor-related and sensory-related inputs preferentially target proximal and distal dendrites of these neurons, respectively. While the majority of inputs are one-to-one, approximately 16% synapse onto multiple targets, forming one-to-many connections. Notably, these shared input patterns extend across different monoaminergic systems, serving as a structural basis for coordinated neuromodulation. Our results demonstrate the organization principles of the NM system's input architecture, particularly within the LC-NE system. This brain-wide, multiplexed molecular annotated microscale reconstruction of a vertebrate brain, combined with multi-modal mesoscopic datasets, offers a reliable resource for the precise identification of diverse neuronal types within EM connectomes, and provides critical reference for elucidating the synaptic architecture principles underlying sensorimotor and NM pathways in the vertebrate brain.

## Keywords

Molecular annotated connectomics, APEX2, mesoscopic-atlas assisted inference, neuromodulatory pathways, LC-NE neurons, zebrafish

## Introduction

Brain function is underpinned by exquisitely organized architectural principles that operate across various scales, ranging from the precise spatial localization of synapses to the intricate morphologies of individual neurons and the characteristic connectivity patterns among distinct brain regions. The synaptic-resolution connectome represents a foundational challenge in neuroscience, offering a mechanistic framework to bridge structure, function, and behavior[1-3]. While complete wiring diagrams have been achieved for small invertebrate nervous systems[4,5], vertebrate whole-brain connectomics remains incomplete — despite landmark achievements including mouse cortical reconstructions[6-14]. Zebrafish (*Danio rerio*) larvae now emerge as the most tractable vertebrate model for whole-brain connectomics, combining manageable brain scale with conserved circuit architecture.

Pioneering work has mapped local circuits[15-18] or generated whole-brain datasets[19,20], yet existing datasets often possess limited resolution or omit essential input – output regions—notably the retina (sensory entry) and spinal cord (motor output)—limiting systems-level interrogation of sensorimotor transformation.

The functional complexity of neural networks arises not only from their physical wiring, but also from the molecular diversity of their constituent neurons. Molecular defined neuronal types serve as crucial bridges linking static structural data with dynamic functional readouts. Recent light-microscopy-based connectomics (LICONN) highlights the field's urgent need for molecular annotated connectomics. Traditional volume electron microscopy (vEM)-based connectomics has primarily relied on prior structural features for neuronal classification, including stereotyped somata positioning, projection morphologies, specialized cellular structures, and synaptic ultrastructures[21]. For neuronal populations with less well-characterized structural signatures, cell-type identification has been achieved mainly through correlative light-electron microscopy (CLEM), genetically encoded tags for EM (GETEM) and immuno-EM. Beyond a few well-studied excitatory and inhibitory populations (e.g., cortical pyramidal neurons and interneurons, zebrafish Mauthner cells and their homologs), the majority of cell types—particularly neuromodulatory populations—lack sufficient ground-truth data for structural feature extraction. For these challenging cases, GETEM currently represent the most robust annotation approach, enabling precise molecular identification within synaptic-resolution wiring diagrams without complex computations.

To address this, we present a brain-wide, synapse-level, multiplexed molecular annotated vEM dataset spanning from the retina to the anterior spinal cord in 6-day post-fertilization (dpf) larval zebrafish. The dataset features noradrenergic, dopaminergic, serotonergic, hypocretinergic/orexinergic, and glycinergic neurons that are genetically labeled using enhanced ascorbate peroxidase 2 (APEX2) targeted to distinct subcellular compartments, driven by cell-type-specific promoters[22-30]. Additionally, glutamatergic and GABAergic neurons are inferred through the Zebrafish Mesoscopic Atlas[31]-assisted skeleton comparison.

The brain possesses a bi-pathway architecture, where sensorimotor pathways operate in parallel with neuromodulatory pathways[32]. Leveraging the unique advantages of our multiplexed molecular annotated dataset, we tackle a fundamental question in bi-pathway processing: where neuromodulatory neurons such as locus coeruleus noradrenergic (LC-NE) neurons receive their upstream inputs[33,34], and how they structure these diverse inputs across their somatodendritic areas. Different neuromodulatory systems, each with varying indegree, display both segregated and convergent innervations to sensory – motor brain regions that exhibit heterogeneity in synapse density and strength. As a pivotal hub for whole-brain activity modulation[35-45], LC-NE neurons integrate brain-wide inputs that are organized in a modality-specific spatial pattern. Notably, noradrenergic, dopaminergic and serotonergic systems share common inputs, revealing a modular inputome architecture that underlies coordinated neuromodulation within both the LC-NE system and across monoaminergic systems. This dataset is integrated into an open-access online platform, serving as a reliable resource for the precise identification of diverse neuronal types within EM

connectomes, while providing critical reference for elucidating the synaptic architecture principles underlying sensorimotor and neuromodulatory pathways in the vertebrate brain.

## Results

### Whole-brain ssEM of APEX2-labeled larval zebrafish

We utilized enhanced ascorbate peroxidase APEX2[25,29], which catalyzes hydrogen peroxide ($H_2O_2$)-dependent polymerization and localized deposition of diaminobenzidine (DAB), to enable simultaneous labeling of multiple molecularly defined neuronal types within individual brains. APEX2 is selectively targeted to distinct subcellular compartments through signal peptide tagging, driven by cell-type-specific promoters. We generated a *Tg(dbh:GAL4FF;UAS:cytosol-APEX2-TagRFP);Tg(hcrt:APEX2-TagRFP-NLS);Tg(glyt2:MITO-APEX2-TagRFP);Gt(vmat2:GAL4FF)* quadruple transgenic fish line using the Tol2 transposon system[46], in which APEX2 is specifically targeted to (i) the cytoplasm in monoaminergic neurons (noradrenergic, dopaminergic, and serotonergic), (ii) the nucleus in hypocretinergic/orexinergic neurons, and (iii) the mitochondria in glycinergic neurons (**Fig.1a and Extended Data Fig.1**).

Using the automated tape-collecting ultramicrotome - scanning electron microscope (ATUM-SEM) approach[20,47], we acquired whole-brain serial-section scanning electron microscopy (ssEM) datasets at $4 \times 4 \times 33$ $nm^3$ per voxel resolution along the rostrocaudal axis, extending from the olfactory epithelium to the anterior spinal cord (third myomere) in a 6-day post fertilization (dpf) APEX2 multiplexed-labeled larva (**Extended Data Fig.2a**). The imaged volumes, generated from 22,901 consecutive ultrathin sections, encompass $3.1160 \times 10^7$ $\mu m^3$ for the brain (**Fig.1b**), $5.5620 \times 10^4$ $\mu m^3$ for the right optic nerve (**Fig.1c**), and $6.0877 \times 10^6$ $\mu m^3$ for the right retina (**Fig.1d**).

In the brain, 176,810 cells were identified through convolutional neural network (CNN)-based auto-segmentation and manual proofreading of the nuclei, while 25,250,468 synapses featuring postsynaptic densities (PSDs) were automatically identified (precision: 85.60±3.205%; recall: 88.37±1.593%; three $8 \times 8 \times 0.99$ $\mu m^3$ test sets). In the right retina, 81,734 cells were manually counted. The brain exhibits a well-defined bilateral symmetric macro-mesoscale organization, with somata and neuropil displaying relative segregation. Somata are predominantly distributed in the medial-dorsal regions (94.59%), while neuropil, which contains most synapses, is primarily localized to the lateral-ventral areas (**Fig.1e and f**). Embedded within both somata and neuropil regions are heterogeneous neuronal tracts of varying diameters that mediate inter-regional signal transmission (**Fig.1g**). Among these, the spinal reticular system and lateral line system exhibit significant myelination, while the optic nerve shows partial myelination (**Fig.1c**). The vascular network responsible for nutrient supply and metabolic waste clearance is predominantly localized within the neuropil region (**Fig.1h**).

We achieved CNN-based automated three-dimensional (3D) reconstruction of the brain (**Extended Data Fig.2b and 2c**). Subsequent manual proofreading via our self-developed Advanced Connectome Engine (ACE) platform enabled the precise reconstruction of multiple APEX2-labeled neuromodulatory (NM) neurons and their synaptic partners, providing the capability to dissect the

152 synaptic connectivity architecture underlying the neuromodulation of sensorimotor pathways by
153 multiple NM systems (**Fig.1i**).
154
155 **Neuron classification via multi-strategy approaches**
156 For cell-type classification, ssEM datasets were registered with the annotated brain template from the
157 Zebrafish Mesoscopic Atlas[31] using a correlative light and electron microscopy (CLEM) pipeline. All
158 176,810 cells were mapped to their respective brain regions. Significant regional variations in
159 somatic density were observed across brain regions. Notably, regions with lower somatic density,
160 including the tectal neuropil (NL) and medial octavolateralis nucleus (MON) in the brain, as well as
161 the inner plexiform layer (IPL) in the retina, represent potential hubs for intensive synaptic
162 interactions (**Extended Data Fig.3a**).
163 We integrated distinct EM-visible signatures with brain region information of somata to classify
164 and quantify APEX2-labeled neurons (**Fig.2a**). In zebrafish, most monoaminergic nuclei are
165 discretely localized. Despite the shared *vmat2*-driven cytoplasmic APEX2 labeling, individual
166 neurons can be classified as noradrenergic, dopaminergic, or serotonergic based on the localization
167 of their somata. Hcrt and Gly neurons were classified based on nuclear- and mitochondrial-localized
168 APEX2, respectively. In total, we identified 12 LC-NE, 56 MO-NE, 38 OB-DA, 22 PT-DA, 44
169 Hyp-DA, 6 Pr-5HT, 110 DRN-5HT, 12 Hcrt, and 4,019 Gly neurons (**Fig.2b and c**). Specifically, due
170 to the abundant population of Gly neurons, we trained a neural network to automatically detect
171 APEX2-labeled mitochondria. All other APEX2-labeled nuclei were manually quantified by expert
172 annotators. Furthermore, we compared these numbers with those from knock-in lines or published
173 lines of corresponding neuronal types, and found that the APEX2-labeled transgenic line used in this
174 study exhibited significant variations in labeling efficiency across different nuclei. For instance, over
175 80% of LC-NE neurons were labeled (Left, n = 5; Right, n =7; The average number per fish, n = 14),
176 whereas pretectal monoaminergic neurons showed minimal labeling, with the few labeled cells
177 primarily being serotonergic neurons (**Extended Data Fig.1c**). These variations may result from
178 either heterogeneous APEX2 expression levels across nuclei or differential DAB penetration
179 efficiency.
180 Next, we tested whether structural features extracted from APEX2-labeled neurons could serve
181 as ground truth to classify corresponding types of neurons lacking APEX2 labeling. Given that most
182 cells remain incomplete fragments after automated reconstruction, neuronal classification based on
183 local structural features allows for the rapid and precise targeting of specific neuronal populations,
184 followed by efficient proofreading[49]. For example, nuclear features alone can distinguish endothelial
185 cells, pericytes, and a subset of glycinergic neurons with nuclear infolding (**Extended Data Fig.3b**
186 **and 3c**). We therefore focused on perisomatic ultrastructures, revealing that most somata in the
187 zebrafish brain contain spherical or ellipsoidal nuclei, typically surrounded by 1 - 2 Golgi apparatus,
188 as well as heterogeneously scaled endoplasmic reticulum and mitochondria (**Fig.2d**). For instance,
189 within LC region, somatic volume and perisomatic mitochondrial number show significant
190 differences between APEX2-labeled NE neurons and adjacent unlabeled cells, enabling precise

discrimination between NE and non-NE cells. According to these criteria, we identified two additional unlabeled LC-NE neurons in the right hemisphere whose morphological features of somatodendritic areas closely match those of the five right APEX2-labeled LC-NE neurons (**Fig.2e and f**). Notably, LC-NE neurons contain significantly greater numbers of perisomatic mitochondria than other labeled neuronal types, suggesting coordinated adaptation between their ultrastructural characteristics associated with energy supply and brain-wide functions (**Fig.2g**).

The extraordinary diversity of molecularly defined neuronal types makes it difficult to generate super-transgenic fish lines with APEX2 targeted to differential subcellular compartments of more neuronal types. We therefore tested whether neuronal types could be inferred by comparing neuronal morphologies between ssEM datasets and the Zebrafish Mesoscopic Atlas, which comprises over 20,000 fully reconstructed glutamatergic and GABAergic neurons (**Fig.2a**). For each query neuron, we extracted mesoscopic data within a 25-μm radius sphere centered at its geometric centroid. Subsequent skeleton matching against these references allowed type inference based on morphological similarity (**Fig.2h-j**). Besides, we found that excitatory and inhibitory synapses exhibit no differences in PSD thickness and volume. These results are consistent with our findings in another sample using mitochondrial APEX2 to label glutamatergic and GABAergic neurons, further demonstrating the feasibility of neuronal skeleton morphology-based type inference (**Extended Data Fig.4**).

## Diversity in region- and neuronal type-specific synapse distribution

Various neuronal types are synaptically interconnected, collectively forming an integrated entity that executes diverse neurophysiological functions. To investigate the connectivity properties of diverse neuronal types, we first systematically characterized all synapses in the brain. To ensure analytical precision, we defined typical synapses by the co-occurrence of PSDs and presynaptic vesicle clouds (SVs). Our analysis revealed substantial heterogeneity in synaptic component (**Fig.3a**). Notably, approximately 41% of synapses lack mitochondria. Given mitochondria's critical roles in energizing synaptic functions, their presence may serve as a potential marker of functional synapses in static EM datasets. We further quantified the numbers and densities of synapses and their three components across brain regions (**Fig.3b and Extended Data Fig.5**), revealing a negative correlation between synaptic distribution and soma distribution (**Fig.3c**). Specifically, synapses are predominantly localized in neuropil regions, while somata regions contain sparse synapses. Interestingly, when we incorporated features associated with synapse strength (including PSD volume and SV volume) into our analysis, we found that synapse strengths across all brain regions follow a log-normal distribution (**Fig.3d-g**). However, the distribution patterns differ among distinct brain regions within sensorimotor pathways, suggesting potential variations in synaptic organization principles. Rarer strong synapses may enable higher signal-to-noise ratios, while more balanced distributions of synapse strengths could enable either more complex neural computations or enhanced plasticity.

As noted previously, neuropil regions serve as the primary sites for synaptic communication, necessitating matched neuromodulation by specific NM systems. Mesoscopic projectome analysis

revealed distinct region-specific innervation patterns among different NM neuronal types (**Extended Data Fig.6**). For example, LC-NE neurons exhibit widespread, broadcast-like projections throughout the brain, while OB-DA neurons demonstrate spatially restricted innervation. Leveraging the synaptic-resolution of ssEM datasets and the multiplexed annotations of neuronal types, we further investigated the relationship between dendritic indegree and innervation scales across diverse neuronal types. We manually reconstructed complete somatodendritic morphologies for multiple neuronal types in the right hemisphere and validated their presynaptic input sites (**Fig.3h and 3i**). Notably, although individual monoaminergic neurons also exhibit varying indegree among themselves, some nuclei significantly exceed those of others (**Fig.3j**). Similarly, Mauthner cells also demonstrate high dendritic indegree, but differ in having abundant inputs on their somata as well. The relationship between dendritic indegree and innervation scales is diversified (**Fig.3j and Extended Data Fig.6**). For some NM neurons, dendritic indegree positively correlates with projection length, where low indegree associate with local neuromodulation (e.g. OB-DA) and high indegree with broad neuromodulation (e.g. LC-NE). In contrast, other NM neurons exhibiting low indegree despite long projection lengths may be responsible for long-range transmission of specific information (Pr-5HT and MO-NE).

## Input organization principles of the LC-NE system

We further manually proofread the presynaptic neurons of multiple NM neurons to delineate their input architecture. As a key node in regulating brain states, the convergent input organization of LC-NE neuronal populations has been revealed by viral-genetic tracing[33,34]. However, how brain-wide inputs conveying distinct physiological information are spatially organized on dendrites remains poorly understood. We reconstructed all presynaptic neurons originating from the 561 dendritic synapses of a single LC-NE neuron (LC-NE 3#) that exhibits the longest dendrites and highest dendritic indegree, successfully tracing 75% of these synaptic inputs (n = 419) back to their somata (**Fig.4a**). Notably, a single LC-NE neuron receives widespread presynaptic inputs from 27 brain regions, with a dominant preference for motor-related regions in hindbrain, particularly in rhombomere 1 (**Fig.4b**). In contrast, some NM neurons (e.g. OB-DA and Pr-5HT) receive inputs that are spatially constrained within unitary neuropil regions, suggesting relatively modality-specific neuromodulation (**Extended Data Fig.7**). Although the LC-NE system is known as multisensory-responsive, we found that it receives sparse direct inputs from canonical visual (12 neurons) and auditory (1 neurons) brain regions. Integrated analysis of synaptic spatial positions and their corresponding somatic locations revealed that LC-NE neurons implement modality-dependent spatial organization of dendritic inputs. Motor-related and sensory-related inputs preferentially target proximal and distal dendrites of these neurons, respectively. They exhibit no significant differences in either PSD volume or SV volume (**Fig.4c and 4d**). This phenomenon was reminiscent of observations in mouse cortical pyramidal neurons, where apical dendritic inputs exert regulatory control over the effects of feedforward inputs targeting proximal dendrites, enabling context-dependent dendritic integration[50].

Recent studies support the heterogeneous and modular organization of the LC-NE system[51-53]. Our results further demonstrate inter-individual heterogeneity in dendritic inputs among LC-NE neurons, with the majority following one-to-one connectivity rules. For instance, we identified that LC-NE 4# specifically receives Hcrt inputs (**Extended Data Fig.8**), while most glycinergic neurons target only single LC-NE neurons. These results reinforce the concept of LC-NE system heterogeneity. We also identified common presynaptic inputs (CPI) that innervate two or more LC-NE neurons (**Fig.4e-g**). Such shared inputs may represent an important neural substrate underlying the synchronous activity observed in LC-NE neuronal populations[35,54,55], potentially serving to coordinate their functional outputs under specific behavioral or physiological conditions. Interestingly, CPIs exhibit varying divergence degrees, with most innervating 2 – 3 LC-NE neurons (**Fig.4h and 4i**). Moreover, we identified inter-monoaminergic shared input patterns. Specific inter-CPIs simultaneously innervate any two of LC-NE, PT-DA, and DRN-5HT neurons (**Fig.4j-m**). These inter-CPIs may constitute the structural basis for coordinated activity across distinct monoaminergic modules, enabling more diversified neuromodulation. In summary, leveraging this cell-type-annotated, synapse-level whole-brain EM datasets, we resolved brain-wide inputs to individual LC-NE neurons, which are spatially organized in a strength- and modality-dependent manner. Furthermore, we identified a shared input mode that recruits LC-NE populations, and even multiple monoaminergic systems, to generate modular neuromodulatory effects with varying intensities and neuromodulator combinations (**Fig.4n**).

## Discussion

In this study, we present a brain-wide, synapse-level, multiplexed molecular annotated vEM dataset of larval zebrafish. The dataset extends beyond the brain to include the unilateral retina, optic nerve, and partial spinal cord, providing a unique resource for investigating sensorimotor transformations, particularly for visual processing pathways.This is particularly valuable considering the zebrafish as a visually dominant species, where the number of cells in a single retina is more than one-third that of the entire brain. While CNN-based automated reconstruction has been completed for the brain, extensive manual proofreading remains essential for achieving a truly validated whole-brain connectome. With ongoing improvements in online collaborative proofreading systems, we can now systematically map input – output architectures of key neuromodulatory systems. Furthermore, rapidly advancing AI-for-Science (AI4S) technologies will enable dataset realignment and resegmentation, significantly enhancing connectome validation efficiency. Importantly, our ATUM-SEM approach has preserved all sectioned samples intact, allowing for future acquisition of currently unmapped extracerebral structures to expand this resource.

Our dataset features multiplexed molecular annotation. Using a subcellular compartment-targeted APEX2 strategy, we have achieved the simultaneous labeling of at least five molecularly defined neuronal types, including four important neuromodulatory neuronal populations across eight corresponding nuclei. For non-APEX2-labeled neuronal classes, such as glutamatergic and GABAergic neurons, we have established a feasible framework for inferring excitatory/inhibitory

(E/I) identities through mesoscopic atlas-assisted skeleton comparison, combined with synaptic ultrastructural features. While perisomatic and synaptic ultrastructural features have been demonstrated to enable precise cell-type identification, vertebrate connectomics has been hampered by the lack of sufficient ground-truth references, particularly for neuromodulatory neurons. Our dataset provides readily identifiable and reliable EM-visible markers, from which structural signatures of corresponding neuronal classes have been extracted. These signatures can not only facilitate the complementary identification of unlabeled individuals within our dataset but also enable broader application to other zebrafish vEM datasets.

This study represents the first successful implementation of multiplexed APEX2 labeling in an intact vertebrate brain. An alternative approach to molecular annotation utilizes CLEM, a method whereby distinct neuronal populations are fluorescently labeled and subsequently correlated with EM data. This approach directly leverages existing zebrafish transgenic lines and typically produces high-quality images, as hydrogen peroxide is not required for sample preparation. In contrast, the GETEM strategy exemplified by APEX2 offers distinct advantages: (i) identifiability without complex registration calculations, (ii) multiplexed molecular annotation through orthogonal multi-compartment labeling that overcomes the spectral constraints of fluorescent proteins, and (iii) suitability for distal/long-range axonal labeling in local EM reconstructions where complete neuronal morphologies are unavailable. Importantly, the above two strategies can be used in combination — the fluorescent signals from APEX2-fused proteins exhibit perfect correspondence with their EM-visible counterparts generated through APEX2 catalysis, serving as matching landmarks that simplify CLEM registration. Furthermore, we demonstrate the feasibility of a molecular annotation strategy based on cross-modal dataset alignment. Compared to vEM, the light-microscopy-based mesoscopic atlas features neuronal type-specific promoter-driven sparse fluorescent labeling, enabling more efficient and cost-effective acquisition of vast datasets containing complete morphological profiles of known neuronal types. By matching the reconstructed skeletons or morphological features (whether partial or complete) from vEM data with these mesoscopic references, we can reliably infer molecular identities. Collectively, these complementary strategies will significantly advance our understanding of structural characteristics across diverse neuronal types, ultimately contributing to the comprehensive reconstruction of a molecular annotated whole-brain connectome in zebrafish.

This study elucidates the significance of molecular annotated connectomics in deciphering brain architecture through the lens of the LC-NE system. As an evolutionarily conserved hub regulating brain-wide states and behavioral performance, the LC-NE system receives convergent inputs and broadcasts information widely, while accumulating evidence reveals its modular functional organization. Through relatively comprehensive reconstruction of presynaptic inputs onto single LC-NE neurons, we demonstrate that individual LC-NE neurons integrate brain-wide inputs exhibiting modality- and strength-specific spatial organization: motor-related inputs with stronger synapse strength preferentially target proximal dendrites, while non-motor-related weaker inputs

predominantly innervate distal dendrites. Whether this proximal－distal dichotomy corresponds to phasic－tonic firing patterns requires further investigation[56]. Similar to cortical pyramidal neurons where apical dendritic inputs modulate proximal inputs, we postulate comparable interactive mechanisms in LC-NE neurons — their activity strongly correlates with motor output, while non-motor-related inputs adjust the gain of motor-related signals, enabling brain-state-dependent modulation. Thus, the LC-NE system not only broadcasts noradrenergic signals globally but also monitors whole-brain activity through extensive inputs to self-tune its regulatory efficacy. The predominantly one-to-one connectivity, along with one-to-many connectivity typically targeting 2－3 LC-NE neurons, further supports functional modularity, whereas rare common inputs innervating most LC-NE neurons, combined with previously reported electrical synapses, may synchronize population activity for specific functions requiring massive norepinephrine release. Shared input patterns across monoaminergic systems reveal combinatorial neuromodulator co-release mechanisms, highlighting complex inter-system interactions and underscoring the value of multiplexed molecular annotated connectomics. Future work will focus on monoaminergic systems to delineate their inputome and outputome organizations underlying coordinated neuromodulation beyond the canonical bi-pathway architecture.

## Method

### Zebrafish husbandry

Adult Zebrafish (*Danio rerio)* were kept in a circulating system at 28℃ under a 14:10 hour light-dark cycle. All animal protocols were reviewed and approved by the Animal Care and Use Committee of the Center for Excellence in Brain Science and Intelligence Technology, Chinese Academy of Sciences (NA-046-2023). Larvae were fed with *Brachionid* rotifers from 4.5 to 9 dpf, then switched to freshly hatched *Artemia* nauplii thereafter. The sex of embryonic and larval zebrafish was undetermined.

### Zebrafish lines

All transgenic zebrafish larvae are in nacre background. The vmat2, dbh, th1, tph2, hcrt, vglut2a, gad1b, glyt2 promoters were used to label monoaminergic, noradrenergic, noradrenergic/dopaminergic, serotonergic, hypocretinergic, glutamatergic, GABAergic, and glycinergic neurons, respectively. Published fish lines used in this study include: *Tg(UAS:mCherry)zf408* (*abbreviation*: *Tg(UAS:mCherry)*) (22904685), *Tg(slc6a5:GFP)cf3* (*Tg(glyt2:GFP)*) (17330042), *Tg(-2.0Fru.Hcrt:EGFP)zf11* (*Tg(Hcrt:EGFP)*) (17182791), *Tg(5 × UAS:EGFP)nkuasgfp1a* (*Tg(5 ×UAS-TATA:EGFP)*) (18202183), *Tg(elavl3:Hsa.H2B-GCaMP6f)jf7* (*Tg(HuC:H2B-GCaMP6f)*) (28425439), *Tg(5 × UAS-hsp70l:GCaMP6s)nkUAShspzGCaMP6s13a* (*Tg(UAS:GCaMP6s)*) (28425439), *Ki1(th:EGFP)ion27d* (*Ki1(th:EGFP)*) (25849248), *Ki(th:GAL4-VP16)ion32d* (*Ki(th:GAL4-VP16)*) (25849248), *Ki(tph2:EGFP)ion39d* (*Ki(tph2:EGFP)*) (25849248), *Ki(dbh:GAL4-VP16)ion36d* (*Ki(dbh:GAL4-VP16)*) (38467902), *Tg(slc17a6:GAL4FF)ion177d* (*Tg(vglut2a:GAL4FF)*) (38467902).

385 *Tg(slc6a5:Hsa.Cox8a-APEX2-TagRFP)ion97d* (*Tg(glyt2:MITO-APEX2-TagRFP)*),
386 *Tg(hcrt:APEX2-TagRFP-NLS)ion100d* (*Tg(hcrt:APEX2-TagRFP-NLS)*) and *Tg(dbh:GAL4FF;5 ×*
387 *UAS-hsp:cytosol-APEX2-TagRFP)ion142d* (*Tg(dbh:GAL4FF;UAS:cytosol-APEX2-TagRFP)*) were
388 all constructed by Dr. Fu-ning Li and Can Shi with Tol2 system.
389 *Ki(tph2:GAL4FF,myl7:EGFP)ion127d* (*Ki(tph2:GAL4FF,cmlc2:EGFP)*) was constructed by Dr.
390 Fu-ning Li.
391

392 **DAB staining**

393 The optimized DAB staining protocol was adapted from published procedures. The 0.1 M Tris-HCl
394 buffer (pH 7.4) was prepared by dissolving 0.6055 g Tris-Base (Millipore, Cat# 648311) in 50 mL of
395 ultrapure water, with pH adjustment using concentrated HCl. A 10 mg tablet of
396 3,3'-diaminobenzidine tetrahydrochloride (DAB·4HCl, Sigma, Cat# D5905) was subsequently
397 dissolved in 10 mL of this buffer through vigorous vortexing under light-protected conditions. The
398 solution was then filtered through a 0.22-μm membrane (Millipore, Millex$^{TM}$-GP 0.22-μm filter, ) to
399 obtain a 1 mg/mL DAB stock solution, which was stored at 4℃ and protected from light. Samples
400 were sequentially rinsed on a 4℃ shaker or on ice with: (1) 0.1 M phosphate buffer (3 × 10 min), (2)
401 Tris-HCl buffer (2 × 10 min), and (3) DAB solution (2 × 10 min) to remove residual aldehydes. For
402 the reaction, 1 μL of 30% $H_2O_2$ (Sinopharm Chemical Reagent Co., Ltd., Cat# 10011218) was mixed
403 with 1 mL DAB stock to prepare the working solution, after which samples were incubated for 2 h at
404 room temperature in complete darkness. The reaction was terminated by washing with Tris-HCl
405 buffer (2 × 10 min). The catalysis by APEX2 of DAB polymerization resulted in dark brown
406 precipitates, which were clearly visible under bright-field stereomicroscopy. Post-fixation with
407 osmium tetroxide was conducted immediately following DAB staining to preserve the osmiophilic
408 reaction products.
409

410 **EM sample preparation**

411 A mixed fixative containing 2% paraformaldehyde (PFA) and 2% glutaraldehyde (GA) was used for
412 effective whole-brain fixation. A 1 mL aliquot of 25% GA (Sigma, Cat# G5882, stored at -20℃) was
413 thawed at 4℃ under light protection. Concurrently, 1 g PFA powder (Sigma, Cat# 158127) was
414 dissolved in 20 mL of ultrapure water within a fume hood, with 1 - 2 drops of 1 M NaOH added. The
415 solution was then sealed, protected from light, and heated at 65℃ with magnetic stirring until fully
416 clarified. After cooling to room temperature, the solution was filtered through a 0.22 μm membrane
417 to yield 5% PFA stock. The 10-mL working fixative was prepared immediately before dissection by
418 mixing 4 mL of 5% PFA, 0.8 mL of 25% GA, 5 mL of 0.1 M phosphate buffer (pH 7.4), and 0.2 mL
419 of ultrapure water. Larvae were embedded in 1.5% low-melting-point agarose (Invitrogen, Cat#
420 15517014) dissolved in extracellular solution (in mM: 134 NaCl, 2.9 KCl, 2.1 $CaCl_2·2H_2O$, 1.2
421 $MgCl_2·6H_2O$, 10 HEPES, 10 glucose; 290 mOsm, pH 7.8). The agarose covering dorsal epidermis
422 and pectoral fins was removed. Using glass micropipettes, the skin was carefully dissected from the
423 hindbrain ventricle while avoiding damage to vascular/neural tissues. The trunk was rapidly

transected anterior to the swim bladder using ophthalmic scissors, after which the head was gently extracted with fine forceps and immediately immersed in fresh fixative. The fixed samples were sealed and stored at 4℃ in darkness overnight. Subsequent procedures followed the standardized rOTO protocol.

## X-ray tomography

We employed X-ray microscopy (XRM) imaging to rapidly and non-destructively assess the quality of whole-brain electron microscopy samples from larval zebrafish. Samples exhibiting uniform staining, minimal deformation, and no apparent mechanical damage were selected for subsequent ultrathin sectioning and scanning electron microscopy imaging. The X-ray microtomography was performed using the Xradia 520 Versa system (Zeiss, Germany) at Shanghai Jiao Tong University's Instrumental Analysis Center. After appropriate resin trimming, samples were scanned at 60 kV with 1 $\mu m^3$ voxel resolution, requiring approximately 2 hours per sample.

Data analysis and visualization were conducted using Dragonfly software (Object Research Systems, Canada). Sequential images were imported with resampling parameters and voxel resolution specified. The sample orientation was adjusted by dragging and rotating reference lines in the display window. Selected views were exported as projection sequences via the "Derive new from current view" function. For 3D visualization, the Video marker tool generated animated sequences that were subsequently exported.

## Collection of whole-brain ultrathin sections

Using an ultramicrotome equipped with an automated tape-collecting system (ATUMtome, RMC, USA), serial sections were obtained with thicknesses ranging from 30 to 35 nm. Prior to collection, trimmed excess blank resin around the larva using a double-edged razor blade. The front guide slot of the ATUMtome was properly positioned, and parameters including sectioning speed (0.8 mm/s), tape-advancing speed (0.6 mm/s), and water refilling interval (5-second durations every 8 minutes) were set. The anti-static device and intermittent water replenishment system were activated to ensure sequential and stable section collection on hydrophilic, conductive polyimide film strips (KAPTON-PET, DuPont, USA). If section instability is observed during collection (e.g., incomplete sections), immediately halt sectioning and either reposition the knife edge or replace the diamond knife.Throughout the process, ambient conditions were maintained at approximately 25℃ and 60% humidity.

Following collection, section-bearing strips were segmented and mounted onto 4-inch monocrystalline silicon wafers using 0.8-mm-wide conductive adhesive tape (SPI, USA), with careful pressing to eliminate air bubbles. The mounted wafer was placed into a LEICA EM ACE600 high-vacuum coater for carbon deposition (6 – 10 nm film thickness). The section surfaces were cleaned using nitrogen gas blowing, and subsequently stored in a dry cabinet at 25℃ and 30% humidity. The constructed whole-brain ultrathin section library of larval zebrafish comprised 22,901 serial sections along the rostrocaudal axis, with an average thickness of 33 nm. The entire collection

process required three days and utilized three diamond knives (UltraMaxi, Diatome, Switzerland).

## SEM image acquisition

The adhered wafers underwent carbon coating first, with a film thickness of 10 nm (Leica, ACE 600, Germany), enhancing the electrical conductivity of the sample surface and minimizing the accumulation of charge. Next, self-developed wafer pre-irradiation equipment was employed, subjecting the entire wafer to irradiation to enhance sample stability and backscattered electron signal contrast. The irradiation was conducted with a current of 9 mA and a voltage of 2000 V for a continuous duration of 10 seconds. The processed wafers were then placed in an optical microscope (FBT, Clippers, China) for the acquisition of navigation images, using a line-scan rapid imaging method with a resolution of 7.6 μm.

Due to the ultra-thin thickness of the sections and the characteristics of resin materials, issues such as contamination, cracks, folds, and even section loss are unavoidable during sectioning, collection, knife-changing, and imaging processes. These problems are particularly pronounced in the zebrafish eye region, primarily due to the significant structural differences between the eye and brain tissues. Statistical analysis revealed that 99 sections in the zebrafish eye area were left unimaged as a result of the aforementioned issues.

High-throughput image acquisition was conducted concurrently across three scanning electron microscopes (FBT, Navigator NeuroSEM100, China), which are facilitated by a bespoke collection software engineered to ensure the utmost efficiency in image output. The pixel resolution was 4 nm, the dwell time was 43.5 ns, and the acceleration voltage was 2 kV. Auto focus and astigmatic correction were set to 80 seconds per section.

To expedite the acquisition rate and enhance the probability of successful imaging, a methodical region-specific focusing coupled with photography was implemented. Firstly, the image ROI of each section was divided into multiple tiles (12,000 × 12,000 pixels) with approximately 10% overlaps, 16 tiles arranged in 4 rows and 4 columns considered as one region. Regions with fewer than 16 tiles at the section edge were also considered as individual standard region. The regions were numbered starting from ‘region1’ and follows a serpentine pattern based on their positions. Secondly, prior to scanning each section, a low-resolution focus was conducted to ensure the algorithm's efficacy in pinpointing the optimal focal range at the center of the section, which was set at a resolution of 50 nm with a dwell time of 80 ns. Subsequently, the stage was precisely oriented to the center of the first region, and high-resolution focusing and astigmatic correction were performed with a resolution of 4 nm and a dwell time of 80 ns. After focusing, the imaging followed a snake-like trajectory for each tile. Upon completion, the stage was shifted to the position of next region, enabling the high-resolution focus and scanning to continue. The ideal time of stage and data transfer to store was 2.5s per tile. This cyclical pattern continues until all regions of the current section were captured, with transitions between regions following a serpentine navigation pattern. The process repeats for subsequent sections until the imaging of the entire wafer was accomplished.

## EM image stitching

The 3D volume registration of EM images was accomplished through two sequential stages: tile stitching followed by section alignment. Each section was divided into a grid of approximately 54 tiles (arranged in 9 rows × 6 columns) at 12,000 × 12,000 pixels per tile. To ensure accurate stitching, the adjacent tiles were acquired with a 12% overlapping region. The stitching workflow proceeded through three computational stages: First, feature detection and matching using Scale-Invariant Feature Transform (SIFT) descriptors extracted from tile overlap regions. Second, pairwise displacement estimation via coordinate transformation analysis. Third, global position optimization through linear least squares minimization. Specifically, SIFT-matched feature point pairs served as the basis for calculating local translation vectors between tiles. To mitigate error accumulation, a global optimization framework simultaneously adjusted all tile positions by minimizing the total displacement error across the entire section, thereby ensuring precise tile stitching within each section.

## EM image alignment

A multi-scale alignment method was implemented to register serial sections through coarse- and fine-scale processing. To address error accumulation, the pipeline employed a sub-volume-division strategy, partitioning the original dataset into 764 spatially coherent stacks (each containing 31 consecutive sections). Continuity across stacks was established by selecting the first section of each stack as a reference section (764 total). These references underwent affine transformation to correct notable deformations while maintaining spatial invariance throughout alignment, serving as stable pivots to prevent cumulative error propagation. Alignment then proceeded within each stack, from coarse to fine scales.

Sections were downsampled 32× during coarse-scale alignment. Correspondences between two adjacent sections were initially extracted using SIFT descriptors and subsequently filtered using the RANSAC algorithm to enhance reliability. Affine transformation was applied to align adjacent sections. Sections were downsampled 8× during fine-scale alignment. Damaged sections were first aligned to their neighbors using an expected affine method . Subsequently, an optimized elastic method generated dense correspondence fields between adjacent sections, guiding the iterative refinement of deformation meshes that balanced local adaptability with global smoothness. Finally, Thin-Plate Spline (TPS) transformations extrapolated these deformations to original-resolution sections, preserving ultrastructural continuity at synaptic resolution.

## Bidirectional CLEM

To match the resolution of the template brain of the Zebrafish Mesoscopic Atlas (1 $\mu m^3$), the 764 reference sections were further downsampled in the xy-plane to generate downsampled whole-brain EM images (992 × 992 × 990 $nm^3$ per voxel) for bidirectional CLEM. Multimodal image registration was accomplished through a three-stage approach: First, whole-brain nuclei were extracted from both the Zebrafish Mesoscopic Atlas and ssEM datasets to create nuclei point clouds, which were

then rigidly aligned using the Iterative Closest Point (ICP) algorithm. Manually-annotated nuclei from four 6-dpf *Tg(elavl3:H2B-GCaMP6f)* larvae were used to generate the average point cloud for the LM template brain, while nuclei from ssEM datasets were automatically segmented. Second, the EM images were globally constrained using X-ray data. Third, computed bidirectional deformation fields between LM and EM spaces through 3D template matching and TPS transformations. Somata regions across the entire brain, along with other EM-identifiable brain regions including pineal gland, pituitary gland, and bilateral optic tectal neuropil regions, were manually annotated on downsampled whole-brain EM images for joint optimization. These annotated regions served as reference landmarks for registration with their well-established counterparts in the template brain of the Zebrafish Mesoscopic Atlas.

## 3D Automatic reconstruction

To ensure the quality of electron microscope imaging, we employ image quality assessment methods for overall control and timely screening of image anomalies such as distortion, blurring, wrinkles, scratches, and tears. Measures such as retaking, reshooting, or replacement are applied to enhance system performance. Simultaneously, defect and effective tissue masks are precomputed to support subsequent analysis. A 2D U-Net network is trained for blur detection, generating quality assessment scores. Experts verify low-scoring images using a developed software tool to determine if retakes are necessary. Effective tissue masks are identified based on EM image grayscale features to prevent defect propagation that may affect downstream computations. By combining manual annotation with CNN-based defect detection, three sub-volumes ($8600 \times 8600 \times 30$ voxels) are labeled as ground truth for effective tissue. The U-Net network classifies voxels into brain, non-brain, and loss areas (e.g., wrinkles, scratches, tears) with a resolution of $32 \times 32 \times 33$ $nm^3$. Detection results are further confirmed by annotators to ensure the accurate identification of regions affected by wrinkles, cracks, and artificial marks caused by diamond knife replacement. All masks collectively form the defect mask, providing a foundation for subsequent image reconstruction.

To address the Poisson and Gaussian noise inherent in electron microscopy (EM) imaging and to overcome the challenges of self-supervised denoising with degraded inputs, we propose a novel framework, Blind2Unblind, for implicit lossless self-supervised denoising. This framework leverages a mask-guided medium to enhance and denoise EM images. It consists of a globally-aware mask mapper driven by mask-based sampling and a non-blind lossless training strategy based on re-visible loss. The denoising network employs the U-Net architecture (Ronneberger et al., 2015), with Adam optimizer (Kingma et al., 2015) and a weight decay coefficient of 1e-8. The initial learning rate is set to 0.001, and the learning rate is halved every 20 epochs within 100 training epochs. The hyperparameters for re-visible loss are set to $\eta = 1$, $\lambda_s = 2$, and $\lambda_f = 20$, based on experimental experience. During training, the EM data is randomly cropped into $128 \times 128$ pixel patches. In practice, the values of blind spot pixels are replaced by the weighted average of their $3 \times 3$ neighboring pixels. This denoising process provides high signal-to-noise ratio (SNR) and

high-fidelity detail for subsequent brain neural atlas reconstruction and EM image analysis, ensuring the integrity and precision of the processed neural tissue slices.

In large-scale ssEM (Serial Section Electron Microscopy) stacks, unavoidable local misalignments during imaging often negatively impact segmentation accuracy. To address this issue, inspired by the Flood-Filling network segmentation pipeline, we propose a local registration strategy that realigns local sub-volumes prior to inference and segmentation. Specifically, we estimate a $4 \times 4$ affine transformation matrix for each sub-volume, which characterizes the geometric transformation of the sub-volume relative to the target space. Each sub-volume is then padded and transformed according to its respective matrix to align it with the global reference space. After the network inference, agglomeration or connected components labeling algorithms, the results are de-aligned and cropped back to the original shape, restoring the spatial consistency of the image. To improve processing efficiency, the affine transformation matrices for all sub-volumes are precomputed and stored prior to processing. This strategy not only significantly reduces computation time but also ensures that high registration accuracy is maintained, even when handling large-scale datasets, preserving local details throughout the process.

In this study, the network used for image segmentation tasks adopts a U-shaped architecture that combines Swin Transformer modules with residual blocks. The network consists of an analysis path with four downsampling layers and a synthesis path with four upsampling layers. The encoder transmits features from each resolution level to the decoder via skip connections, with downsampling performed through block merge layers. The decoder upsamples features using deconvolution and skip connections, ultimately generating segmentation output through a $1\times1\times1$ convolution followed by a sigmoid activation. This architecture balances local and global feature modeling while ensuring computational efficiency, leading to accurate segmentation results. Each layer of the network includes three convolutions (with consistent padding), followed by batch normalization and ReLU activation, all connected via residual skip connections. To enhance data diversity and improve model generalization, several data augmentation techniques were employed. These include image rotations and reflections in eight directions, mirror padding, random cropping, and elastic deformations. Additionally, methods such as CutBlur, CutNoise, and Mixup were incorporated to further strengthen the model’s robustness against noise and anomalies. To further improve the model's adaptability, various image anomalies were simulated, including registration offsets, motion blur, partial 2D slice loss, and incomplete 3D image sequences. These simulated anomalies allow the model to better handle potential quality issues in real-world data, thus enhancing the accuracy and stability of segmentation results.

A block-based strategy was designed for parallel network inference on the complete dataset. The original image is divided into overlapping sub-volumes, which are distributed across more than 20 nodes in a Spark cluster, each equipped with four NVIDIA® GeForce RTX 4090 GPUs. Each sub-volume is first padded and realigned, then cropped into smaller overlapping blocks. After network inference, a Gaussian bump function is applied to merge the overlapping probability maps. The final predictions for each sub-volume are then realigned, cropped, and saved. For tasks such as

neuron segmentation, synapse detection, and mitochondrial identification, the block and overlap sizes are set to 8600×8600×31 and 600×600×1 pixels, with a resolution of 4×4×33 $nm^3$. For tasks like cell nucleus detection and vessel recognition, the block and overlap sizes are set to 1075×1075×31 and 75×75×1 pixels, with a resolution of 32×32×33 $nm^3$. In this study, a block-based connected component labeling (CCL) process is designed for parallel 3D labeling, similar to the block-based network inference strategy. The entire dataset is divided into multiple sub-volumes, distributed across 20 nodes in a Spark cluster, with each node equipped with 112 CPUs. Each sub-volume is first padded and realigned, and then agglomeration or CCL algorithms is applied to perform 3D instance labeling. Afterward, the 3D instance maps of each sub-volume are realigned, cropped, and saved. Once all sub-volumes are processed, adjacent sub-volumes are merged based on shared boundaries to form the final composite 3D instance map.

This study employs a boundary detection-based method for dense segmentation of the zebrafish whole-brain dataset. A three-dimensional network is used to predict three neighboring affinity maps, which are then post-processed using the Distance Transform Watershed (DTW) algorithm to generate superpixels for each slice. The network training is accelerated using eight NVIDIA A100 40G GPUs. The training data consists of seven sub-volumes, each formed by randomly selecting consecutive images from the entire dataset. Each sub-volume has a size of 2000×2000×30 pixels with a resolution of 4×4×33 $nm^3$, and all data are annotated by experienced human experts to ensure high-quality training. 3D image blocks of size 256×256×16 are cropped and input into the network to predict the corresponding three neighboring affinity maps. The loss function used in this study is a composite loss, combining weighted cross-entropy and Dice loss to achieve better segmentation results for imbalanced data. During training, a linear warm-up and cosine annealing learning rate scheduler is applied, with an initial learning rate of 0.01 and 500,000 iterations. To merge over-segmented neuron fragments, an aggregation method based on Region Adjacency Graph (RAG) is employed. During this process, accurately reconstructed nuclei and synapse results, verified by manual inspection, are introduced as prior information to guide the correct merging of neuron fragments.

## Nucleus clustering

Nuclei often exhibit highly diverse and irregular 3D shapes, posing significant challenges for computational analysis. To address this, we developed a comprehensive feature extraction pipeline that integrates both traditional handcrafted morphological features and high-level representations learned through self-supervised learning. Volumetric EM data were first processed using the CloudVolume framework to compute 3D surface meshes for all nuclei (N = 176,239). We then extracted 15 handcrafted morphological features from each nucleus mesh M using the Trimesh library. These features quantitatively describe the size, shape, and geometric properties of individual nuclei. To complement these interpretable handcrafted features, we implemented a self-supervised deep learning framework to extract high-level geometric representations of nucleus shape. Unlike voxel- or mesh-based formats, point clouds offer a compact and resolution-independent

representation that preserves fine morphological details. The point clouds were processed using a Siamese self-supervised architecture based on SimSiam to learn transformation-invariant descriptors. To reduce redundancy and enable integration with handcrafted features, we applied Uniform Manifold Approximation and Projection (UMAP).

## PSD, SV, and mitochondria segmentation

We trained a three-class 3D U-Net to predict the synaptic clefts and vesicle clouds at the downsampled resolution of 8nm * 8nm * 33nm. Four regions with different tissues was cropped and manually annotated by multiple rounds as the groud truth, encompassing 146M voxels. The network was optimized using a multi-class cross-entropy loss and a Stochastic Gradient Descent (SGD) optimize. During training, a warmup learning rate strategy with a initial learning rate of 0.01, linear warmup of 2k steps and cosine decay for total training steps of 500k. We also conducted the data augmentation to improve the robustness of network, including the random rotation, random flip, grayscale transformation, elastic transformation and blur simulation. To test the network performance, we manually annotated another three regions as the test sets. The evaluation against the test sets yielded an average precision of 85.8% and an average recall of 81.4%.

A 3D U-Net was trained to detect the mitochondria at the resolution of 8nm * 8nm * 33nm of the whole dataset. We annotated five sub-volumes as the ground truth, totaling 467M voxels. To separate the adjacent mitochondria, we designed the network to predict the mitochondrial mask and the instance boundary mask at the same time. The mitochondrial mask channel was trained using binary cross-entropy loss, while instance boundary mask channel was optimized with the combination of binary cross-entropy loss and dice loss. Training was conducted for 500k iterations using a SGD optimizer, with a learning rate scheduling strategy identical to that employed in the synapse detection task. The data augmentation techniques were also configured consistently with those applied in the synapse detection framework.

## Proofreading

Extensive manual, semi-automated proofreading of the multi-scale segmentation improved the accuracy of the neural circuit reconstruction. ACE (Advanced Connectome Engine) is a specialized software solution designed for reconstructing large-scale neural data. It integrates massive data management, intelligent computing, and collaborative tools. Utilizing its engineering-driven process management, it guarantees efficient and accurate reconstruction of connectomes. The data management system based on Hadoop and Hbase allows the construction of elastic and secure distributed clusters of computers for the storage and fast retrieval of large-scale connectome data, including ssEM image, neuron reconstruction result, and so on.

In the proofreading system, the data structure of the neuron reconstruction result is defined as a graph structure that connects the segmentation contours of each layer belonging to a neuron on the serial sections. Such a data structure allows us to improve proofreading efficiency by comparing the segmentation contours of adjacent layers to locate abnormal positions in the reconstruction results,

and guide the proofreaders to proofread. In order to efficiently manage the entire proofreading project and control the proofreading quality of the proofreaders, we embedded a project management module in the proofreading system. This module carries out unified management of proofreading tasks, provides a collaborative proofreading environment for the proofreaders, and records the basic operation and the comparison of proofreading results of each proofreader, so as to grasp the dynamics of the proofreaders in a timely manner.

We utilized a series of foundation models for segmentation, specifically the Segment Anything Model (SAM), SAM 2 and SAEM², to aid our proofreading workflow. Based on these models, we further implemented two extra strategies to enhance the human-computer interaction of our software: (1) The SAM ViT-H model checkpoint was exported to an ONNX model with additional quantization and optimization. We then used ONNXRuntime (https://onnxruntime.ai/docs/) on CPU or GPU to execute these models, which not only supports cross-platform ONNX model inference but also improves software runtime. (2) The SAM embeddings generated by the encoders were precomputed and saved in the CloudVolume (https://github.com/seung-lab/cloud-volume) "kempressed" format, which had been tested to have a higher compression ratio than "raw", "fpzip" and others (https://github.com/seung-lab/cloud-volume/wiki/Advanced-Topic:-fpzip-and-kempressed-Encodings).

For 2D semi-automated segmentation, we took manually traced neuron skeletons with (optional) extra positive and negative points as input prompts for the SAM model. However, the pretrained SAM still cannot accurately segment the dense and homogeneous axons and dendrites of neurons in the brain. Thus, we proposed the finetuned SAEM² with auxiliary tasks to acquire complementary multi-head information for neuron segmentation in volume EM. Here, the auxiliary task was cell boundaries (i.e., plasma membranes), supplementing the original SAM, which only focuses on cell masks.

For 3D semi-automated segmentation, we further implemented the SAM 2 with two extra strategies: (1) We learned to predict cross-correlation maps and then calculated the shifts between adjacent 2D EM images. (2) We used the distance transformation maps of the previous cell masks to sample prompt points of the next cell masks.

## Micro-mesoscopic skeleton comparison

Cross-scale skeleton matching aims to establish correspondences between the same type of neurons under different imaging modalities, based on the spatial distances between two reconstructed skeletons. The skeleton of a single neuron ($S_L$) in optical microscopy is complete, whereas EM reconstruction provides a partial skeleton of the same neuron ($S_E$). Therefore, $S_E$ is set as the reference, and the matching similarity is constructed by calculating the unidirectional distance to $S_L$. Specifically, the distance D between $S_L$ and $S_E$ is calculated as:

$$D = \frac{1}{|S_E|} \sum_{p \in S_E} D_{min}(p, S_L)$$

where $D_{min}$ represents the shortest distance from $S_L$ to the point p in $S_E$. This distance is calculated for each point in $S_E$, and the average is taken. The $S_L$ that minimizes D is selected as the most similar skeleton corresponding to $S_E$.

## 3D Visualization

Following open-science principles, we utilized the Neuroglancer (https://github.com/google/neuroglancer) Precomputed format and CloudVolume interface to manage our data, which is known to be readily available for 3D visualization via Neuroglancer and webKnossos. We used the "jpeg" for volume EM images, "compressed_segmentation" for the silhouette of regions and segmentation of different structures.

We further implemented the Igneous for multiprocessed block-wise downsampling, skeletonization and meshing with the following agglomeration. For skeletonization, we used the Kimimaro (https://github.com/seung-lab/kimimaro) implementation of the automated TEASAR algorithm. We then merged the skeleton splits that may appear based on nearest Euclidean neighbors, calculated the path length of the skeleton, and determined the radius of each vertex in the skeleton. For meshing, we used the automated block-wise Zmesh (https://github.com/seung-lab/zmesh) to generate multi-resolution meshes. These skeletons and meshes are stored in sharded formats.

After the data preparation described above, we used meshes to visualize brain regions and neuron reconstructions, and used annotation points to demonstrate input/output synaptic locations in the Neuroglancer. Besides, we used the Neuroglancer "matrix" as an affine transformation to move, flip, rotate and zoom the original Neuroglancer layer. Note that we were using the parallel projection during Neuroglancer rendering in order to have 3D scale bars. Furthermore, we optimized two existing workflows to make videos: (1) the Neuroglancer with Python scripts of "video_tool", and (2) the open-source computer graphics software Blender (https://www.blender.org/download/lts/) with Python scripts and JSON descriptions of neuVid (https://github.com/connectome-neuprint/neuVid).

## Statistical analysis

Mann Whitney U test was used in Fig.4a. $p^{***} < 0.001$.

## Acknowledgement

We are grateful to Xu-long Wen, and other staffs from Grand View (Beijing) Technology Co., Ltd, Zhi Zeng, Le Wang and other staffs from Chengdu Huizhong Tianzhi Tech. Co., Ltd. (www.hztzai.com) for massive manual proofreading and management, Dr. Yu Kong, Dr. Xu Wang, Li-jun Pan, Xue Xu for assistance in sample preparation, Drs. Ke Zhang, Yun-feng Hua, Jun Zhang, Dan-qian Liu, Yu Mu, Kai Yang, and Sheng-xiong Wang for insightful advice on sample preparation and research direction, the Transdisciplinary Platform of Functional Connectome and Brain-inspired

Intelligence in Huairou Science City in Beijing and the Microscopic Technology & Analysis Center at the Institute of Automation, Chinese Academy of Sciences for providing technical support and device resources, Dr. Jie He for providing the *TgBAC(gad1b:GAL4-VP16)*, Dr. Misha Ahrens for providing the *Tg(elavl3:H2B-GCaMP6f)*, Dr. Koichi Kawakami for providing *Tg(UAS:GCaMP6s)*, *Tg(5×UAS-TATA:EGFP)* and *Gt(vmat2:GAL4FF)*, Dr. Joe Fetcho for providing the *Tg(glyt2:GFP)*, Ming-quan Chen, Hong-li Wan and other staffs from Facility of Mapping Brain-Wide Mesoscale Connectome for assistance in utilizing the Zebrafish Mesoscopic Atlas and BrAVe, Jia-wen Huang, Liu-qin Qian, Chen-xi Jin and other staffs from the Big Data of Brain Atlas Facility for establishing a web-sharing platform, Dr. Qian Hu for optical imaging and image processing support, Dr. Chun-feng Shang, Dr. Rong-wei Zhang, Dr. Jia Li, Dr. Yu-fan Wang, Dr. Sha Li, Dr. Le Sun, Yu-chen Gong, Yu Qian, Dr. Qiu-sui Deng, Li-jun Chen for research discussions, and Ji-wen Bu, Ye Hua, Shi-rong Jin, Ning-xin Ren for Fish Facility management. This work was supported by National Science and Technology Innovation 2030 Major Program of the Ministry of Science and Technology (2021ZD0204500, 2021ZD0204502 and 2021ZD0204503), Creative Research Groups (32321003) and general grant (32171461) of the National Natural Science Foundation of China, Shanghai Municipal Science and Technology Major Project (18JC1410100 and 2018SHZDZX05), and Key Research Program of Frontier Sciences (QYZDYSSW-SMC028) and Strategic Priority Research Program (XDB32010200) of Chinese Academy of Sciences.

## Author contributions

J.D. and H.H. conceived and supervised the project. F.L. generated APEX2-labeled fish lines, prepared EM samples, organized proofreading and daily discussions, and drafted the manuscript. J.L. performed the automatic reconstruction of this ssEM dataset, including nucleus segmentation. C.S. generated APEX2-labeled fish lines, prepared EM samples, analyzed the input organization of the LC-NE system, and was responsible for fish line management. J.Y. and L.S. were responsible for proofreading system maintenance and data management. Y.L. and X.C. performed image alignment and CLEM. J.L. performed the automatic segmentation of PSD, SV, and mitochondria. L.Z. was responsible for image acquisition. L.L. collected all ultrathin sections. H.Z. conducted skeletonization and 3D visualization. B.C. handled image denoising and enhancement. Y.Z. executed nucleus clustering. H.C., S.C., and F.Z. participated in image alignment. H.Y. and J.Z. carried out micro-mesoscopic skeleton comparison. H.M. performed ion milling. T.X. was responsible for wrinkle restoration. X.D. assisted in section collection. L.L. also contributed to image acquisition. X.Z. supported remote proofreading management. Z.F. and Y.W. participated in proofreading. C.Z., P.X., and Y.Y. conducted functional investigations of the LC-NE system. X.D. supported the utilization of the Zebrafish Mesoscopic Atlas.

## Declaration of interests

The authors declare no conflict of interest.

808 **Figure legends**

809 **Fig.1 Multiplexed cell-type-labeled whole-brain ssEM of Zebrafish**

810 **a,** A brief EM sample preparation protocol for APEX2-labeled larvae. Larvae are incubated in 1
811 mg/mL DAB solution containing 10 mM $H_2O_2$ (diluted from 30% stock), followed by reduced
812 osmium-thiocarbohydrazide-osmium (rOTO) staining[48]. Subcellular-localized APEX2 catalyzes the
813 conversion of DAB into osmiophilic substances, creating localized, non-transmembrane electron
814 densities within specific neuronal types and generating distinct EM-visible patterns. See methods for
815 a detailed ssEM protocol.

816 **b,** Rendering of the intact larval brain from this study (992 × 992 × 660 $nm^3$ per voxel resolution)
817 generated from original EM images acquired at approximately 400 × 400 × 1,650 $nm^3$ per voxel
818 resolution. Processing included linear interpolation, registration to high-resolution whole-brain EM
819 data, and grayscale equalization. See methods for details.

820 **c,** A representative EM image of the optic nerve in coronal section. **c1**, the expanded view of
821 numerous parallel retinal ganglion cell axons.

822 **d,** A representative EM image of the retina in coronal section.

823 **e,** Rendering of all nuclei distributed across four representative horizontal planes along dorsal-ventral
824 axis (interval: 50 μm). Z represents the dorsoventral distance relative to the epidermal surface.

825 **f,** Rendering of major neuronal tracts in the brain.

826 **g,** Rendering of the vascular network in the brain. Most vasculature remained well-preserved, though
827 some collapse was observed in telencephalic vessels and the basal communicating artery (BCA).

828 **h,** Rendering of incomplete reconstructions of 529 manually-proofread neurons from this study
829 covering majority of brain-wide regions. This includes retinal ganglion cells (RGC, n = 3),
830 noradrenergic neurons in locus coeruleus and medulla oblongata (orange; LC-NE, n = 12; MO-NE, n
831 = 2), dopaminergic neurons in olfactory bulb, posterior tuberculum, and hypothalamus (light green;
832 OB-DA, n = 2; PT-DA, n = 4; Hc-DA, n = 2), serotonergic neurons in pretectum and dorsal raphe
833 nucleus (dark blue; Pr-5HT, n = 2; DRN-5HT, n = 4), hypocretinergic/orexinergic neurons in
834 hypothalamus (purple; Hcrt, n = 2), glycinergic neurons in hindbrain (sky blue; Gly, n = 22),
835 presynaptic partners of several monoaminergic neurons (n = 478), and one Mauthner cell (white).
836 Scale bars: b, d, e, f, g, h, 50 μm; c, 10 μm, 2 μm (expanded); e, 2% (nucleus distribution ratio).

837

838 **Fig.2 Genetic labeling and Mesoscopic Atlas-based neuron classification**

839 **a,** Schematic diagram of multi-strategy approaches for neuron classification.

840 **b,** Representative EM images of all APEX2-labeled neuronal types (left) and their corresponding
841 coronal sections (right). Individual labeled neurons are marked by white asterisks.

842 **c,** Quantification of APEX2-labeled neurons and their ratio to the theoretical population size.
843 Theoretical neuron counts for each type were derived from the average of manual counts across three
844 individuals.

845 **d,** Rendering of a single LC-NE neuron's perisomatic ultrastructures, including nucleus (green),
846 nucleolus (orange), endoplasmic reticulum (brown), Golgi apparatus (dark red), mitochondria (dark

847 blue), and a primary cilia.
848 **e,** Within the LC region, comparisons of volume ratio and somatic mitochondrial density between
849 APEX2-labeled NE neurons and adjacent unlabeled cells. Orange, blue, and gray dots represent
850 APEX2-labeled LC-NE neurons, speculated non-labeled LC-NE neurons, and other cells,
851 respectively.
852 **f,** Rendering of somatodendritic areas of five APEX2-labeled and 2 speculated LC-NE neurons.
853 **g,** Comparisons of somatic mitochondrial number across multiple APEX2-labeled neuronal types.
854 **h,** Representative examples of partially EM-reconstructed neurons paired with their fully
855 LM-reconstructed glutamatergic counterparts.
856 **i,** Representative examples of partially EM-reconstructed neurons paired with their fully
857 LM-reconstructed GABAergic counterparts. The E/I identity of top 10 candidates are displayed in
858 the bottom-left panel, and both the highest-ranking matched cell and the top-scoring unmatched cell
859 are shown.
860 **j,** The relationship between the minimum penalty score and the score difference separating the
861 top-matched cell from the highest-ranking unmatched cell. Corresponding cells in Fig.2h and 2i are
862 indicated by color-coded arrows.
863 Scale bars: b, 1 μm (uncropped image 50 μm); d, 5 μm; f, 20 μm.
864
865 **Fig.3 Scale-distinct innervation exerted by various NM neurons with heterogeneous indegree**
866 **a,** The co-occurrence of PSDs (25.25 million), SVs (15.77 million), and mitochondria (13.73
867 million).
868 **b,** Synapse density distribution across major brain regions in the whole brain.
869 **c,** The relationship between synapse density and cell density across major brain regions.
870 **d,** The distribution of PSD, SV, and mitochondrial volumes across the whole brain.
871 **e,** The distribution of PSD volumes across major brain regions.
872 **f,** The distribution of SV volumes across major brain regions.
873 **g,** The distribution of mitochondrial volumes across major brain regions.
874 **h,** Rendering of EM reconstructions for multiple APEX2-labeled neurons' somatodendritic areas.
875 **i,** Rendering of multiple APEX2-labeled neurons' somatodendritic areas with presynaptic inputs
876 marked.
877 **j,** Summary of dendritic indegree distribution across multiple neuronal types.
878 Scale bars: h, 50 μm; i, 20 μm.
879
880 **Fig.4 Spatial organization and shared mode of LC-NE input architecture**
881 **a,** Rendering of all 419 EM-reconstructed presynaptic neurons with identified somata targeting LC-3.
882 Presynaptic neurons without traced somata were excluded from visualization.
883 **b,** Regional distribution of presynaptic neurons. Brain regions are manually classified as
884 sensory-related (red) and motor-related (blue).
885 **c,** 2D spatial distribution of dendritic inputs on LC-NE 3#. Inputs are manually classified as

886 sensory-related (red) and motor-related (blue) according to their somatic locations.
887 **d,** Spatial distribution of dendritic input strength and modality. Input strength is quantified based on
888 PSD and SV volumes. Mann Whitney U test was performed for statistical analysis.
889 **e,** Rendering of all 72 EM-reconstructed intra-CPIs with identified somata.
890 **f,** Regional distribution of intra-CPIs. Brain regions are manually classified as sensory-related (red)
891 and motor-related (blue).
892 **g,** The proportion of intra-CPI-originating inputs among all LC-NE 3# inputs.
893 **h,** A representative example of intra-CPIs that innervates all 5 APEX2-labeled LC-NE neurons.
894 **i,** The proportion of intra-CPIs with varying divergence degrees.
895 **j,** Rendering of all 26 EM-reconstructed inter-CPIs with identified somata.
896 **k,** Regional distribution of inter-CPIs. Brain regions are manually classified as sensory-related (red)
897 and motor-related (blue).
898 **l,** The proportion of inter-CPI-originating inputs among all LC-3 inputs.
899 **m,** Different shared innervation combinations.
900 **n,** Schematic diagram of dendritic input architecture in the LC-NE system.
901

## Supplemental figure legends

### Extended Data Fig.1 Validation of the APEX2-labeled fish line

**a,** The fluorescent images of the 6-dpf quadruple transgenic larva used for multiplexed labeling in this study. Left, schematic illustrations of APEX2-labeled patterns; Middle, a Z-projected whole-brain fluorescent image; Right, three expanded images showing APEX2-positive neurons in olfactory bulb (dopaminergic, cytoplasmic-localized), hypothalamus (hypocretinergic/orexinergic, nuclear-localized), and hindbrain (glycinergic, mitochondrial-localized), respectively.

**b,** Immunohistochemical validation of LC-NE neuron genetic labeling in 6-dpf *Gt(vmat2:GAL4FF);Tg(dbh:GAL4FF;UAS:cytosol-APEX2-TagRFP)* larvae using tyrosine hydroxylase antibody (anti-TH). Top, TagRFP; Middle, anti-TH; Bottom, merged.

**c,** Immunohistochemical validation of PT-DA neuron genetic labeling in 6-dpf *Gt(vmat2:GAL4FF);Tg(dbh:GAL4FF;UAS:cytosol-APEX2-TagRFP)* larvae using tyrosine hydroxylase antibody. Immunohistochemical validation of Hcrt neuron genetic labeling in 6-dpf *Tg(hcrt:APEX2-TagRFP-NLS)* larvae using hypocretin antibody (anti-Hcrt). Validation of DRN-5HT neuron genetic labeling through fluorescence co-localization analysis comparing with 6-dpf *Ki(tph2:EGFP)* larvae. Validation of Pr-5HT neuron genetic labeling through fluorescence co-localization analysis comparing with 6-dpf *Ki(tph2:EGFP)* larvae. Validation of Gly neuron genetic labeling through fluorescence co-localization analysis comparing with 6-dpf *Tg(glyT2:GFP)* larvae. Top, TagRFP; Middle, reference; Bottom, merged.

Scale bars: a, 50 μm; b-g, 10 μm.

### Extended Data Fig.2 The detailed workflow for ssEM

**a,** The workflow includes live confocal fluorescence imaging, DAB staining, rOTO staining, dehydration, resinification, X-ray micro-tomography, ATUM-SEM, image stitching, 3D registration, and automated 3D reconstruction. See methods for details.

**b,** Rendering of a randomly selected 2.7% (4,731) of all automatically reconstructed cells within the brain.

**c,** Magnified rendering of 1,533 automatically reconstructed cells in bilateral optic tectum.

Scale bars: b, c, 50 μm.

### Extended Data Fig.3 Brain-wide cell type diversity

**a,** Nucleus density distribution across major brain regions in the whole brain.

**b,** UMAP visualization of nuclear clustering of all cells (n = 176,789) in the brain using combined deep-learned and traditional features. Various cell types are color-coded: endothelial cells, pericytes, . See methods for details. Endothelial cells, pericytes, Hcrt neurons, and three types of monoaminergic neurons were manually annotated. Gly neurons were automatically annotated by algorithm through mitochondrial APEX2 identification. 70,114 cells, whose automatically reconstructed supervoxels possess at least one synapse, were presumed as neurons. The remaining were presumed to be glial cells, or neurons embedded in somata regions which processes were not well automatically

941 reconstructed.
942 **c,** Representative EM images showing various cell types, with their nuclei highlighted.
943 Scale bars: c, d, e, f, g, h, 2 μm.
944
945 **Extended Data Fig.4 Synapse classification via mitochondrial APEX2-labeled E/I samples**
946 **a,** Schematic diagram of labeling glutamatergic and GABAergic neurons using mitochondrial
947 APEX2.
948 **b,** Representative EM images of APEX2-labeld mitochondria in glutamatergic neurons. The
949 *5×UAS-2×Cox8a-APEX2-TagRFP* plasmid was transiently expressed in *Tg(vglut2a:GAL4FF)* larvae
950 at 6 dpf to generate mitochondrial APEX2-labeling in glutamatergic neurons.
951 **c,** Representative EM images of APEX2-labeld mitochondria in GABAergic neurons. The
952 *5×UAS-2×Cox8a-APEX2-TagRFP* plasmid was transiently expressed in *TgBAC(gad1b:GAL4-VP16)*
953 larvae at 6 dpf to generate mitochondrial APEX2-labeling in GABAergic neurons.
954 **d,** Comparisons of ultrastructural features between excitatory and inhibitory synapses (E, n = 101; I,
955 n = 116) from mitochondrial APEX2-labeled glutamatergic and GABAergic neurons.
956 Scale bars: b, c, 200 nm.
957
958 **Extended Data Fig.5 Region-specific distributions of PSDs, SVs, and mitochondria**
959 **a,** PSD density distribution across major brain regions in the whole brain.
960 **b,** SV density distribution across major brain regions in the whole brain.
961 **c,** Mitochondrial density distribution across major brain regions in the whole brain.
962
963 **Extended Data Fig.6 Single-cell mesoscopic projectome of multiple NM neuronal types**
964 **a,** A representative example of the mesoscopic morphology of a single LC-NE neuron. The
965 predominantly innervated neuropil is highlighted in light blue.
966 **b,** A representative example of the mesoscopic morphology of a single PT-DA neuron.
967 **c,** A representative example of the mesoscopic morphology of a single DRN-5HT neuron.
968 **d,** A representative example of the mesoscopic morphology of a single MO-NE neuron.
969 **e,** A representative example of the mesoscopic morphology of a single Hcrt neuron.
970 **f,** A representative example of the mesoscopic morphology of a single OB-DA neuron.
971 **g,** A representative example of the mesoscopic morphology of a single Hc-DA neuron.
972 **h,** A representative example of the mesoscopic morphology of a single Pr-5HT neuron.
973
974 **Extended Data Fig.7 EM-reconstruction of inputs to OB-DA and Pr-5HT neurons**
975 **a,** Rendering of a single EM-reconstructed OB-DA neurons' somatodendritic areas and its
976 presynaptic neurons (n = 9) with identified somata. Presynaptic neurons without traced somata were
977 excluded from visualization.
978 **b,** Rendering of a single EM-reconstructed Pr-5HT neurons' somatodendritic areas and its
979 presynaptic neurons (n = 24) with identified somata. Presynaptic neurons without traced somata were

980 excluded from visualization.
981 Scale bar: a, 10 μm; b, 15 μm.
982
983 **Extended Data Fig.8 EM-reconstruction of inputs to LC-NE neurons**
984 Rendering of EM-reconstructed presynaptic inputs (n = 40) to LC-4 with identified somata. Two
985 hypocretinergic presynaptic neurons labeled by nuclear APEX2 are highlighted (magenta).
986

## Reference


1. Boulanger-Weill J, Kämpf F, Schuhknecht GFP, et al. Correlative light and electron microscopy reveals the fine circuit structure underlying evidence accumulation in larval zebrafish. Preprint. *bioRxiv*. 2025;2025.03.14.643363. Published 2025 Jun 1. doi:10.1101/2025.03.14.643363
2. Dorkenwald S, Matsliah A, Sterling AR, et al. Neuronal wiring diagram of an adult brain. *Nature*. 2024;634(8032):124-138. doi:10.1038/s41586-024-07558-y
3. Brittin CA, Cook SJ, Hall DH, Emmons SW, Cohen N. A multi-scale brain map derived from whole-brain volumetric reconstructions. *Nature*. 2021;591(7848):105-110. doi:10.1038/s41586-021-03284-x
4. Lichtman JW, Pfister H, Shavit N. The big data challenges of connectomics. *Nat Neurosci*. 2014;17(11):1448-1454. doi:10.1038/nn.3837
5. Cook SJ, Jarrell TA, Brittin CA, et al. Whole-animal connectomes of both Caenorhabditis elegans sexes. *Nature*. 2019;571(7763):63-71. doi:10.1038/s41586-019-1352-7
6. MICrONS Consortium. Functional connectomics spanning multiple areas of mouse visual cortex. *Nature*. 2025;640(8058):435-447. doi:10.1038/s41586-025-08790-w
7. Celii B, Papadopoulos S, Ding Z, et al. NEURD offers automated proofreading and feature extraction for connectomics. *Nature*. 2025;640(8058):487-496. doi:10.1038/s41586-025-08660-5
8. Gamlin CR, Schneider-Mizell CM, Mallory M, et al. Connectomics of predicted Sst transcriptomic types in mouse visual cortex. *Nature*. 2025;640(8058):497-505. doi:10.1038/s41586-025-08805-6
9. Wang EY, Fahey PG, Ding Z, et al. Foundation model of neural activity predicts response to new stimulus types. *Nature*. 2025;640(8058):470-477. doi:10.1038/s41586-025-08829-y
10. Ding Z, Fahey PG, Papadopoulos S, et al. Functional connectomics reveals general wiring rule in mouse visual cortex. *Nature*. 2025;640(8058):459-469. doi:10.1038/s41586-025-08840-3
11. Dorkenwald S, Schneider-Mizell CM, Brittain D, et al. CAVE: Connectome Annotation Versioning Engine. *Nat Methods*. 2025;22(5):1112-1120. doi:10.1038/s41592-024-02426-z
12. Schneider-Mizell CM, Bodor AL, Brittain D, et al. Inhibitory specificity from a connectomic census of mouse visual cortex [published correction appears in Nature. 2025 Jun;642(8066):E9. doi: 10.1038/s41586-025-09133-5.]. *Nature*. 2025;640(8058):448-458. doi:10.1038/s41586-024-07780-8
13. Gour A, Boergens KM, Heike N, et al. Postnatal connectomic development of inhibition in mouse barrel cortex. *Science*. 2021;371(6528):eabb4534. doi:10.1126/science.abb4534
14. Ngai J. BRAIN 2.0: Transforming neuroscience. *Cell*. 2022;185(1):4-8. doi:10.1016/j.cell.2021.11.037
15. Vishwanathan A, Sood A, Wu J, et al. Predicting modular functions and neural coding of behavior from a synaptic wiring diagram. *Nat Neurosci*. 2024;27(12):2443-2454. doi:10.1038/s41593-024-01784-3
16. Friedrich RW, Wanner AA. Dense Circuit Reconstruction to Understand Neuronal Computation:

1026 Focus on Zebrafish. *Annu Rev Neurosci*. 2021;44:275-293.
1027 doi:10.1146/annurev-neuro-110220-013050
1028 17. Vishwanathan A, Daie K, Ramirez AD, Lichtman JW, Aksay ERF, Seung HS. Electron
1029 Microscopic Reconstruction of Functionally Identified Cells in a Neural Integrator. *Curr Biol*.
1030 2017;27(14):2137-2147.e3. doi:10.1016/j.cub.2017.06.028
1031 18. Wanner AA, Genoud C, Masudi T, Siksou L, Friedrich RW. Dense EM-based reconstruction of
1032 the interglomerular projectome in the zebrafish olfactory bulb. *Nat Neurosci*.
1033 2016;19(6):816-825. doi:10.1038/nn.4290
1034 19. Svara F, Förster D, Kubo F, et al. Automated synapse-level reconstruction of neural circuits in
1035 the larval zebrafish brain. *Nat Methods*. 2022;19(11):1357-1366.
1036 doi:10.1038/s41592-022-01621-0
1037 20. Hildebrand DGC, Cicconet M, Torres RM, et al. Whole-brain serial-section electron microscopy
1038 in larval zebrafish. *Nature*. 2017;545(7654):345-349. doi:10.1038/nature22356
1039 21. Eckstein N, Bates AS, Champion A, et al. Neurotransmitter classification from electron
1040 microscopy images at synaptic sites in Drosophila melanogaster. *Cell*.
1041 2024;187(10):2574-2594.e23. doi:10.1016/j.cell.2024.03.016
1042 22. Zhang Q, Lee WA, Paul DL, Ginty DD. Multiplexed peroxidase-based electron microscopy
1043 labeling enables simultaneous visualization of multiple cell types. *Nat Neurosci*.
1044 2019;22(5):828-839. doi:10.1038/s41593-019-0358-7
1045 23. Cruz-Lopez D, Ramos D, Castilloveitia G, Schikorski T. Quintuple labeling in the electron
1046 microscope with genetically encoded enhanced horseradish peroxidase. *PLoS One*.
1047 2018;13(7):e0200693. Published 2018 Jul 16. doi:10.1371/journal.pone.0200693
1048 24. Shigemoto R, Joesch M. The genetic encoded toolbox for electron microscopy and
1049 connectomics. *Wiley Interdiscip Rev Dev Biol*. 2017;6(6):10.1002/wdev.288.
1050 doi:10.1002/wdev.288
1051 25. Martell JD, Deerinck TJ, Lam SS, Ellisman MH, Ting AY. Electron microscopy using the
1052 genetically encoded APEX2 tag in cultured mammalian cells. *Nat Protoc*. 2017;12(9):1792-1816.
1053 doi:10.1038/nprot.2017.065
1054 26. Joesch M, Mankus D, Yamagata M, et al. Reconstruction of genetically identified neurons
1055 imaged by serial-section electron microscopy. *Elife*. 2016;5:e15015. Published 2016 Jul 7.
1056 doi:10.7554/eLife.15015
1057 27. Ariotti N, Hall TE, Rae J, et al. Modular Detection of GFP-Labeled Proteins for Rapid Screening
1058 by Electron Microscopy in Cells and Organisms. *Dev Cell*. 2015;35(4):513-525.
1059 doi:10.1016/j.devcel.2015.10.016
1060 28. Böhm UL, Prendergast A, Djenoune L, et al. CSF-contacting neurons regulate locomotion by
1061 relaying mechanical stimuli to spinal circuits. *Nat Commun*. 2016;7:10866. Published 2016 Mar
1062 7. doi:10.1038/ncomms10866
1063 29. Lam SS, Martell JD, Kamer KJ, et al. Directed evolution of APEX2 for electron microscopy and
1064 proximity labeling. *Nat Methods*. 2015;12(1):51-54. doi:10.1038/nmeth.3179

30. Atasoy D, Betley JN, Li WP, et al. A genetically specified connectomics approach applied to long-range feeding regulatory circuits. *Nat Neurosci*. 2014;17(12):1830-1839. doi:10.1038/nn.3854
31. Du XF, Yue ZF, Wei JF, et al. Central nervous system atlas of larval zebrafish constructed using the morphology of single excitatory and inhibitory neurons. Preprint. *bioRxiv*. doi: 10.1101/2025.06.06.658008.
32. Li FN, Zhang CM, Du JL. Neuromodulatory processing in the bi-pathway brain architecture. *Curr Opin Neurobiol*. Published online May 23, 2025. doi:10.1016/j.conb.2025.103055
33. Schwarz LA, Miyamichi K, Gao XJ, et al. Viral-genetic tracing of the input-output organization of a central noradrenaline circuit. *Nature*. 2015;524(7563):88-92. doi:10.1038/nature14600
34. Schwarz LA, Luo L. Organization of the locus coeruleus-norepinephrine system. *Curr Biol*. 2015;25(21):R1051-R1056. doi:10.1016/j.cub.2015.09.039
35. Zhang CM, Yang YX, Li FN, et al. Multiple-level organizational logic of the locus coeruleus-norepinephrine system in structure and function. Preprint. *bioRxiv*. doi: 10.1101/2025.06.11.659024.
36. Poe GR, Foote S, Eschenko O, et al. Locus coeruleus: a new look at the blue spot. *Nat Rev Neurosci*. 2020;21(11):644-659. doi:10.1038/s41583-020-0360-9
37. Zerbi V, Floriou-Servou A, Markicevic M, et al. Rapid Reconfiguration of the Functional Connectome after Chemogenetic Locus Coeruleus Activation. *Neuron*. 2019;103(4):702-718.e5. doi:10.1016/j.neuron.2019.05.034
38. Chandler DJ, Jensen P, McCall JG, Pickering AE, Schwarz LA, Totah NK. Redefining Noradrenergic Neuromodulation of Behavior: Impacts of a Modular Locus Coeruleus Architecture. *J Neurosci*. 2019;39(42):8239-8249. doi:10.1523/JNEUROSCI.1164-19.2019
39. Foote SL, Berridge CW. New developments and future directions in understanding locus coeruleus - Norepinephrine (LC-NE) function. *Brain Res*. 2019;1709:81-84. doi:10.1016/j.brainres.2018.09.033
40. Totah NK, Neves RM, Panzeri S, Logothetis NK, Eschenko O. The Locus Coeruleus Is a Complex and Differentiated Neuromodulatory System. *Neuron*. 2018;99(5):1055-1068.e6. doi:10.1016/j.neuron.2018.07.037
41. Sara SJ. The locus coeruleus and noradrenergic modulation of cognition. *Nat Rev Neurosci*. 2009;10(3):211-223. doi:10.1038/nrn2573
42. Bouret S, Sara SJ. Network reset: a simplified overarching theory of locus coeruleus noradrenaline function. *Trends Neurosci*. 2005;28(11):574-582. doi:10.1016/j.tins.2005.09.002
43. Aston-Jones G, Cohen JD. An integrative theory of locus coeruleus-norepinephrine function: adaptive gain and optimal performance. *Annu Rev Neurosci*. 2005;28:403-450. doi:10.1146/annurev.neuro.28.061604.135709
44. Berridge CW, Waterhouse BD. The locus coeruleus-noradrenergic system: modulation of behavioral state and state-dependent cognitive processes. *Brain Res Brain Res Rev*. 2003;42(1):33-84. doi:10.1016/s0165-0173(03)00143-7

45. Usher M, Cohen JD, Servan-Schreiber D, Rajkowski J, Aston-Jones G. The role of locus coeruleus in the regulation of cognitive performance. *Science*. 1999;283(5401):549-554. doi:10.1126/science.283.5401.549
46. Kawakami K. Tol2: a versatile gene transfer vector in vertebrates. *Genome Biol*. 2007;8 Suppl 1(Suppl 1):S7. doi:10.1186/gb-2007-8-s1-s7
47. Hayworth KJ, Morgan JL, Schalek R, Berger DR, Hildebrand DG, Lichtman JW. Imaging ATUM ultrathin section libraries with WaferMapper: a multi-scale approach to EM reconstruction of neural circuits. *Front Neural Circuits*. 2014;8:68. Published 2014 Jun 27. doi:10.3389/fncir.2014.00068
48. Hua Y, Laserstein P, Helmstaedter M. Large-volume en-bloc staining for electron microscopy-based connectomics. *Nat Commun*. 2015;6:7923. Published 2015 Aug 3. doi:10.1038/ncomms8923
49. Elabbady L, Seshamani S, Mu S, et al. Perisomatic ultrastructure efficiently classifies cells in mouse cortex. *Nature*. 2025;640(8058):478-486. doi:10.1038/s41586-024-07765-7
50. Suzuki M, Larkum ME. General Anesthesia Decouples Cortical Pyramidal Neurons. *Cell*. 2020;180(4):666-676.e13. doi:10.1016/j.cell.2020.01.024
51. Uematsu A, Tan BZ, Ycu EA, et al. Modular organization of the brainstem noradrenaline system coordinates opposing learning states. *Nat Neurosci*. 2017;20(11):1602-1611. doi:10.1038/nn.4642
52. Hirschberg S, Li Y, Randall A, Kremer EJ, Pickering AE. Functional dichotomy in spinal- vs prefrontal-projecting locus coeruleus modules splits descending noradrenergic analgesia from ascending aversion and anxiety in rats. *Elife*. 2017;6:e29808. Published 2017 Oct 13. doi:10.7554/eLife.29808
53. Chandler DJ, Gao WJ, Waterhouse BD. Heterogeneous organization of the locus coeruleus projections to prefrontal and motor cortices. *Proc Natl Acad Sci U S A*. 2014;111(18):6816-6821. doi:10.1073/pnas.1320827111
54. Ishimatsu M, Williams JT. Synchronous activity in locus coeruleus results from dendritic interactions in pericoerulear regions. *J Neurosci*. 1996;16(16):5196-5204. doi:10.1523/JNEUROSCI.16-16-05196.1996
55. Christie MJ, Williams JT, North RA. Electrical coupling synchronizes subthreshold activity in locus coeruleus neurons in vitro from neonatal rats. *J Neurosci*. 1989;9(10):3584-3589. doi:10.1523/JNEUROSCI.09-10-03584.1989
56. Grimm C, Duss SN, Privitera M, et al. Tonic and burst-like locus coeruleus stimulation distinctly shift network activity across the cortical hierarchy. *Nat Neurosci*. 2024;27(11):2167-2177. doi:10.1038/s41593-024-01755-8

1140 **Fig.1**

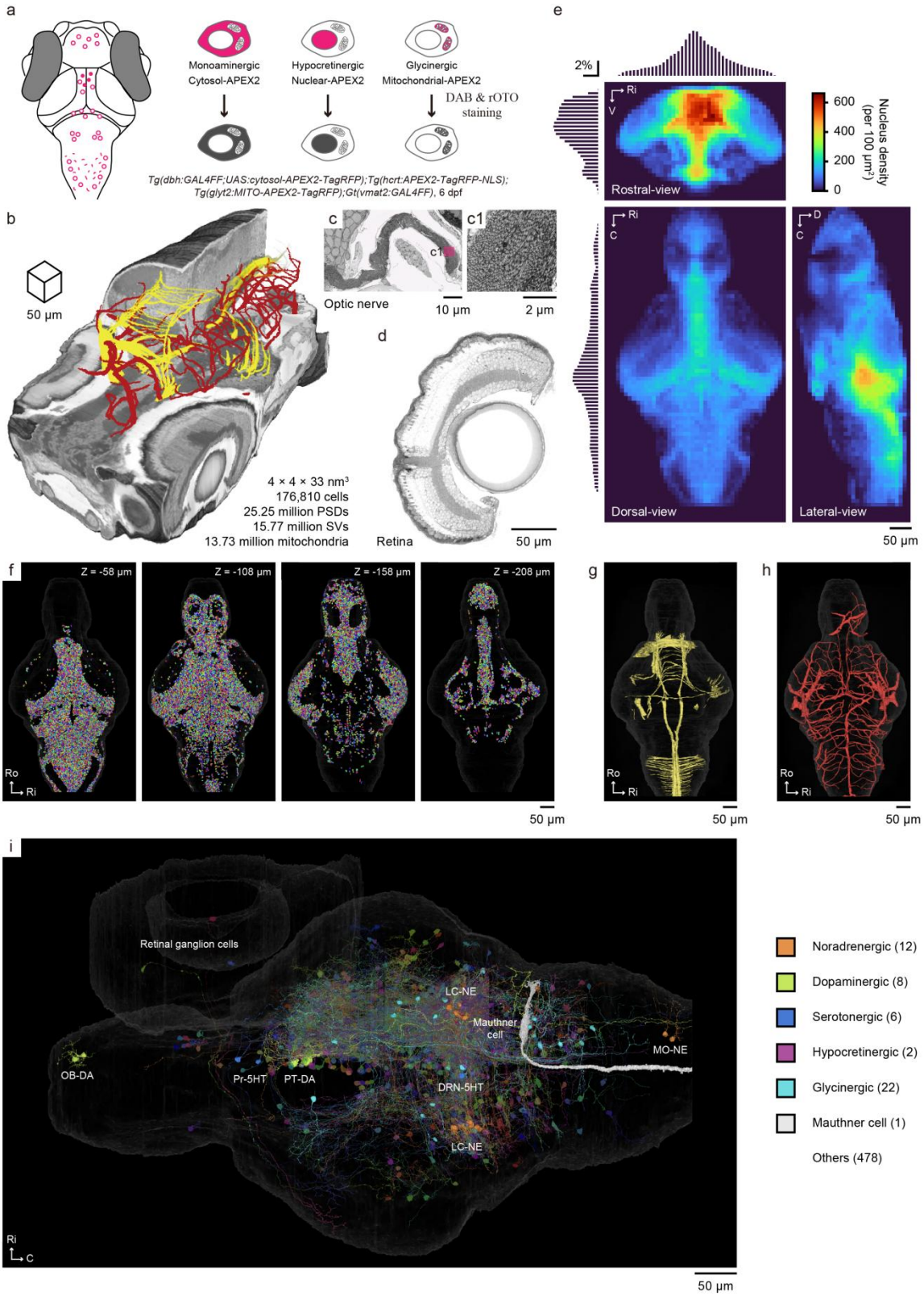


1141

1142

1143 **Fig.2**

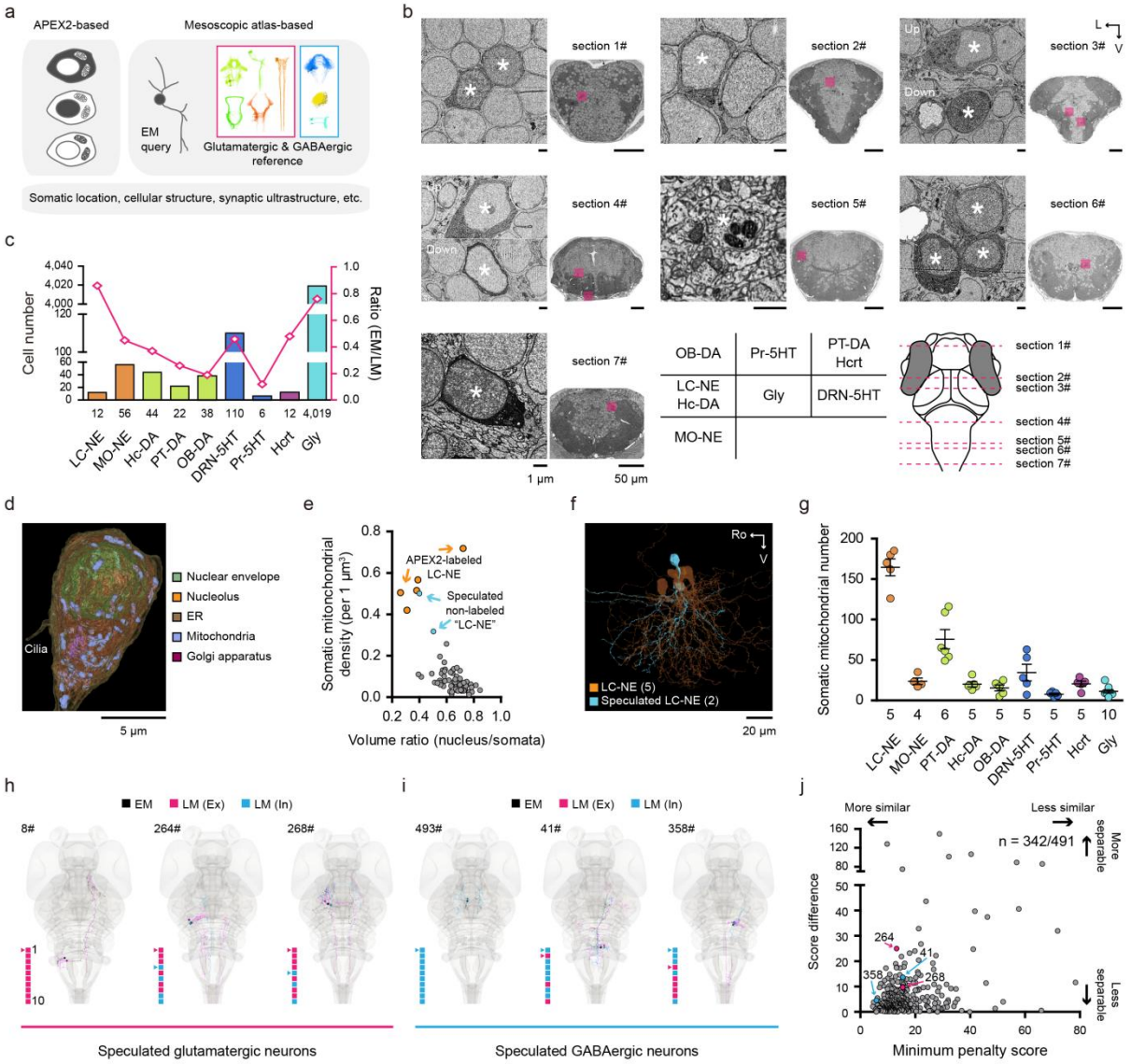


1144

1145

**Fig.3**

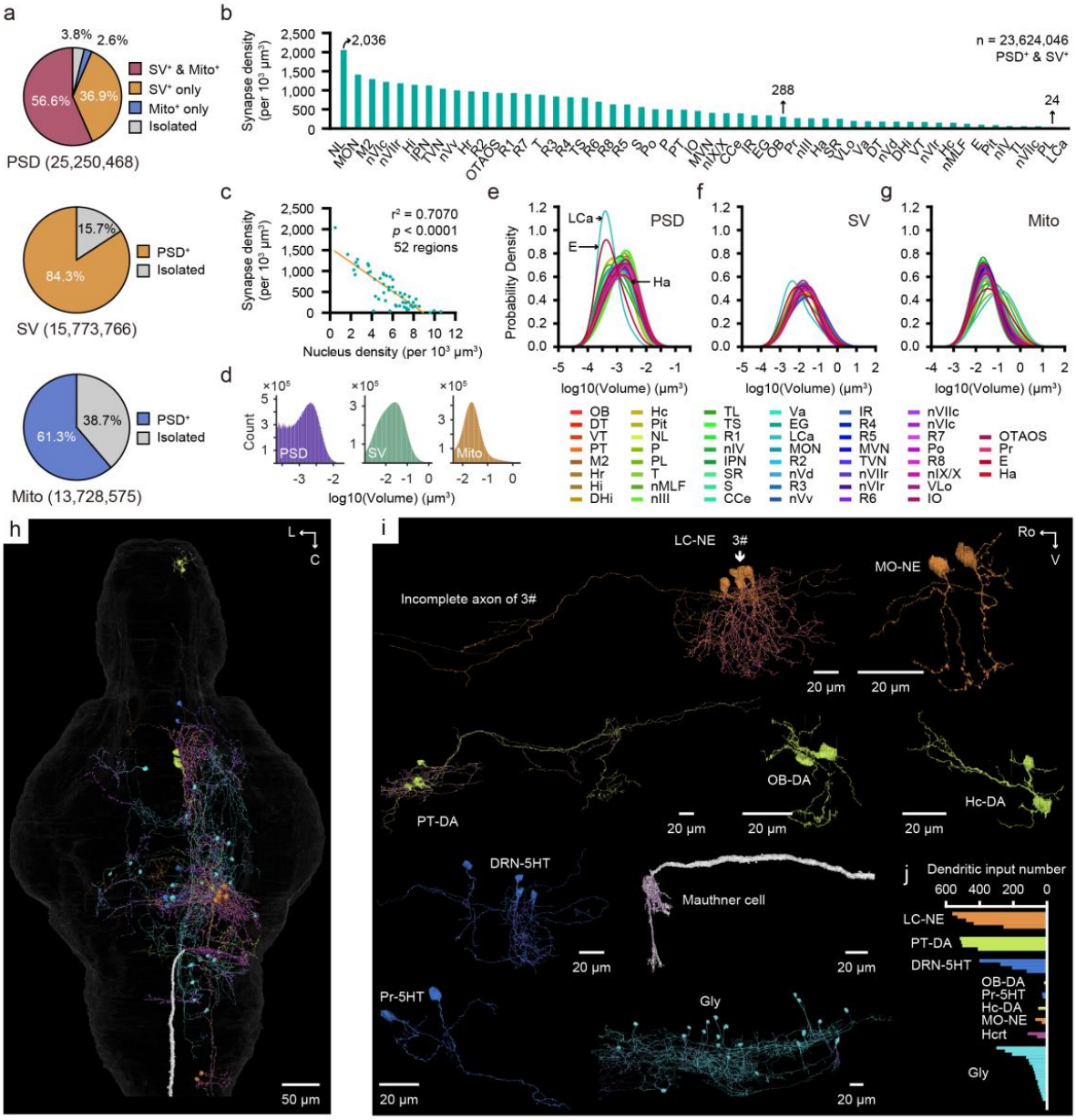
a
3.8%
2.6%
56.6%
36.9%
SV⁺ & Mito⁺
SV⁺ only
Mito⁺ only
Isolated
PSD (25,250,468)
15.7%
84.3%
PSD⁺
Isolated
SV (15,773,766)
38.7%
61.3%
PSD⁺
Isolated
Mito (13,728,575)
b
Synapse density (per 10³ μm³)
2,036
288
24
n = 23,624,046
PSD⁺ & SV⁺
c
r² = 0.7070
p < 0.0001
52 regions
Nucleus density (per 10³ μm³)
d
Count
PSD
SV
Mito
log10(Volume) (μm³)
e
f
g
Probability Density
LCa
E
Ha
PSD
SV
Mito
log10(Volume) (μm³)
OB
DT
VT
PT
M2
Hr
Hi
DHi
Hc
Pit
NL
P
PL
T
nMLF
nIII
TL
TS
R1
nIV
IPN
SR
S
CCe
Va
EG
LCa
MON
R2
nVd
R3
nVv
IR
R4
R5
MVN
TVN
nVIIr
nVIr
R6
nVIIc
nVIc
R7
Po
R8
nIX/X
VLo
IO
OTAOS
Pr
E
Ha
h
L
C
50 μm
i
LC-NE
3#
Incomplete axon of 3#
MO-NE
Ro
V
20 μm
PT-DA
OB-DA
Hc-DA
DRN-5HT
Mauthner cell
Pr-5HT
Gly
j
Dendritic input number
600
400
200
0
LC-NE
PT-DA
DRN-5HT
OB-DA
Pr-5HT
Hc-DA
MO-NE
Hcrt
Gly

1149 **Fig.4**

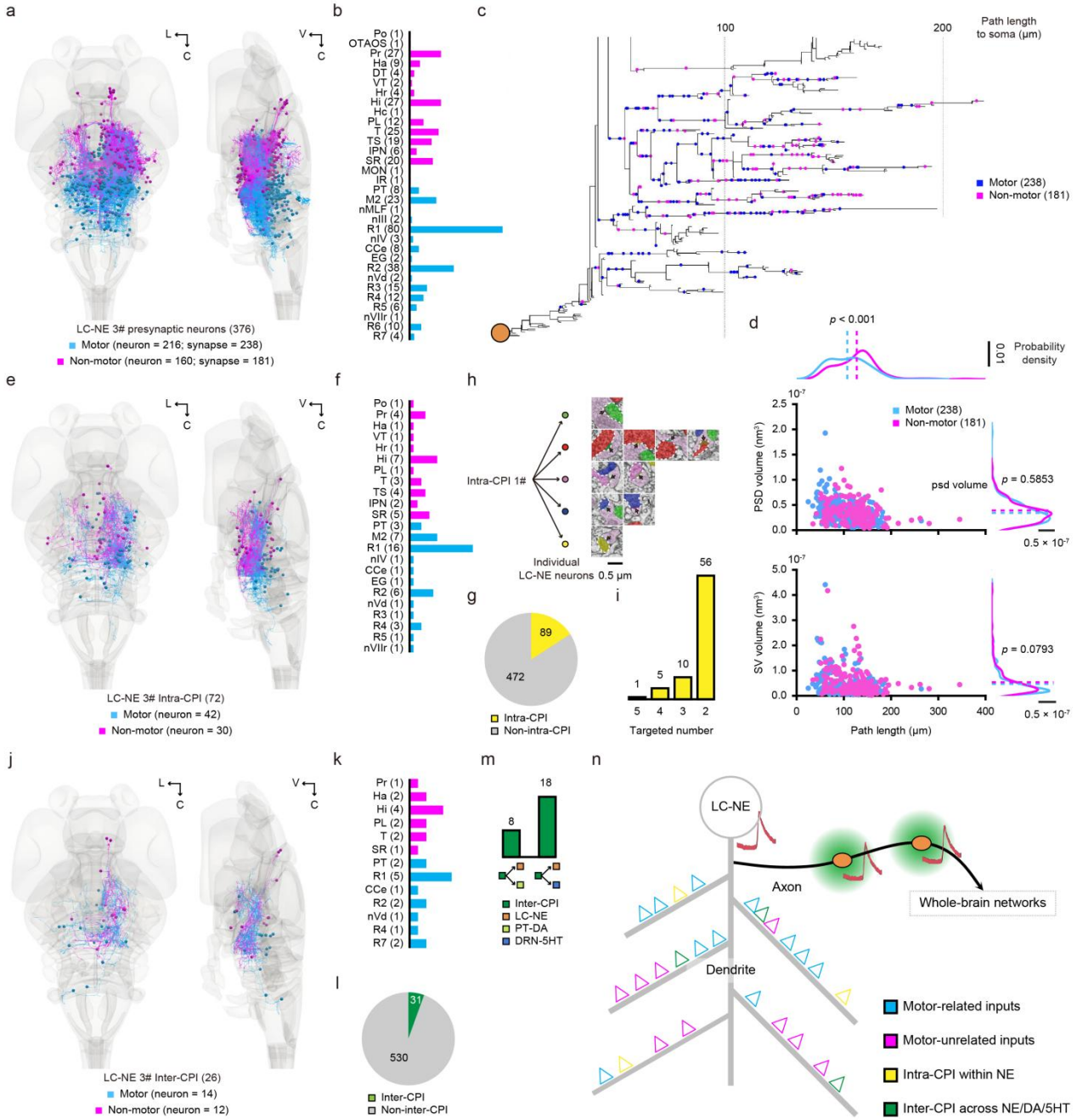


1150

1151

1152 **Extended Data Fig.1**

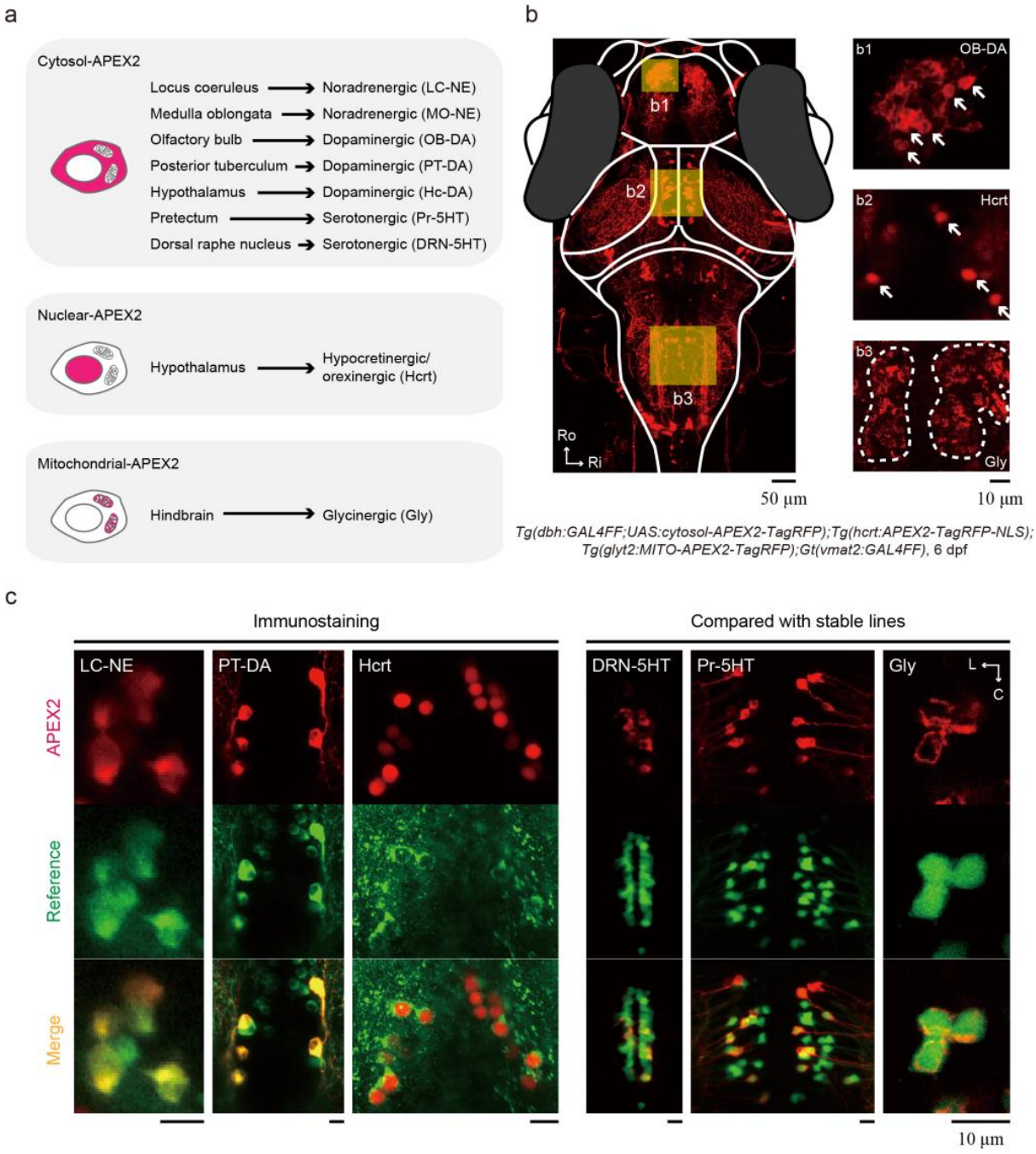


1153

1154

1155 **Extended Data Fig.2**

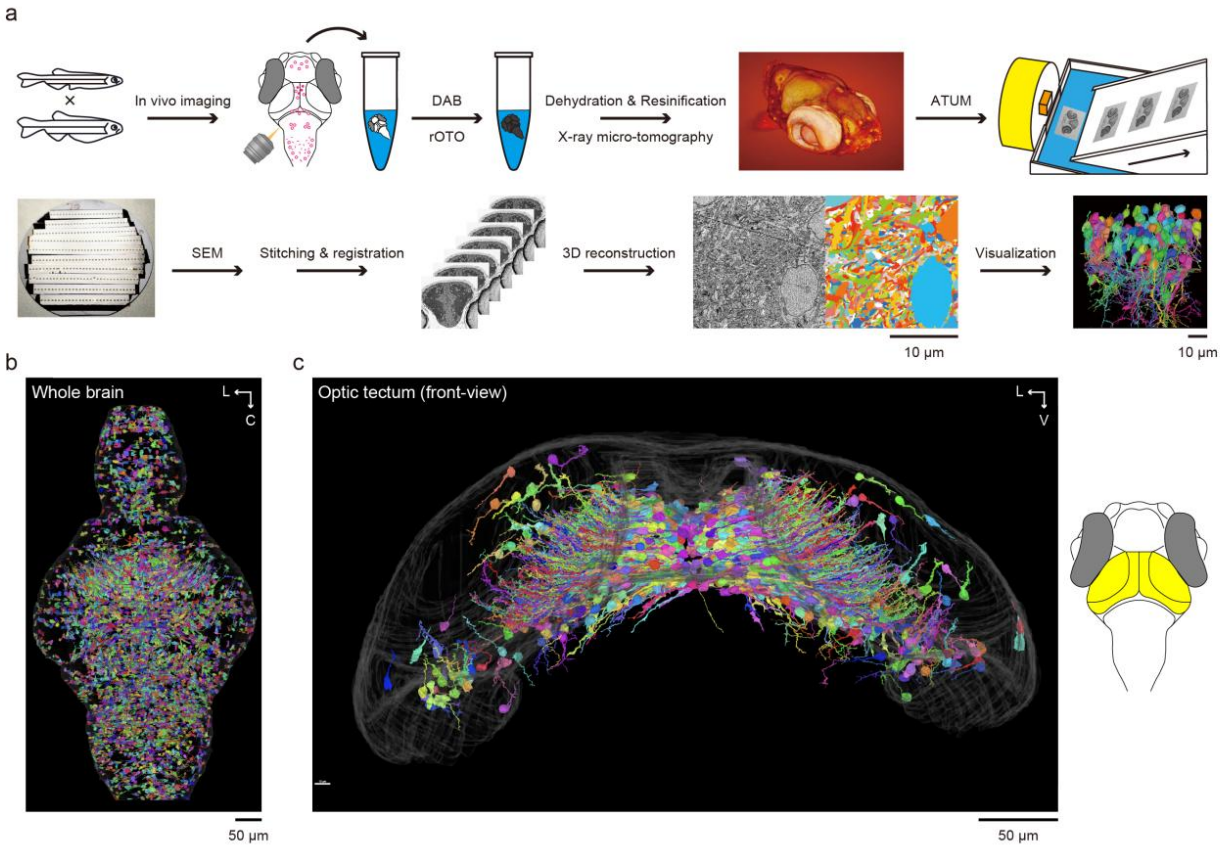


1156

1157

1158 **Extended Data Fig.3**

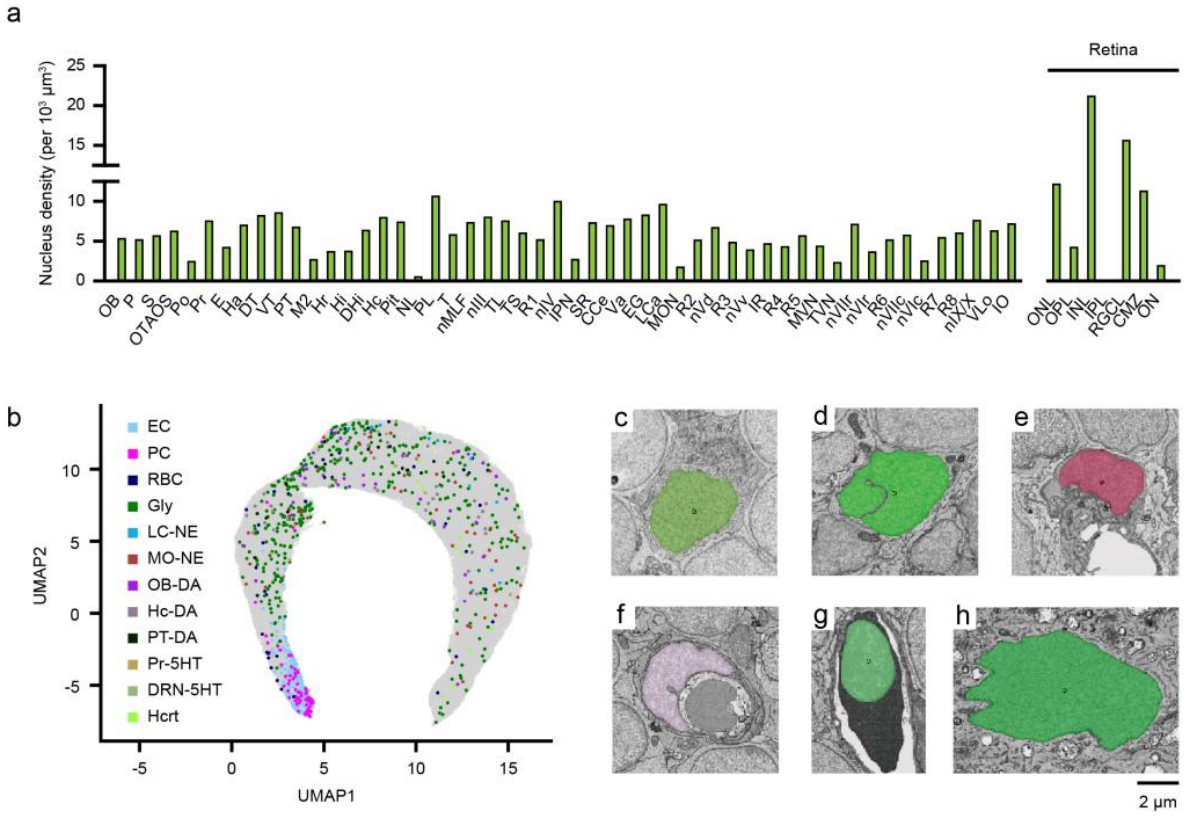


1159
1160

1161 **Extended Data Fig.4**

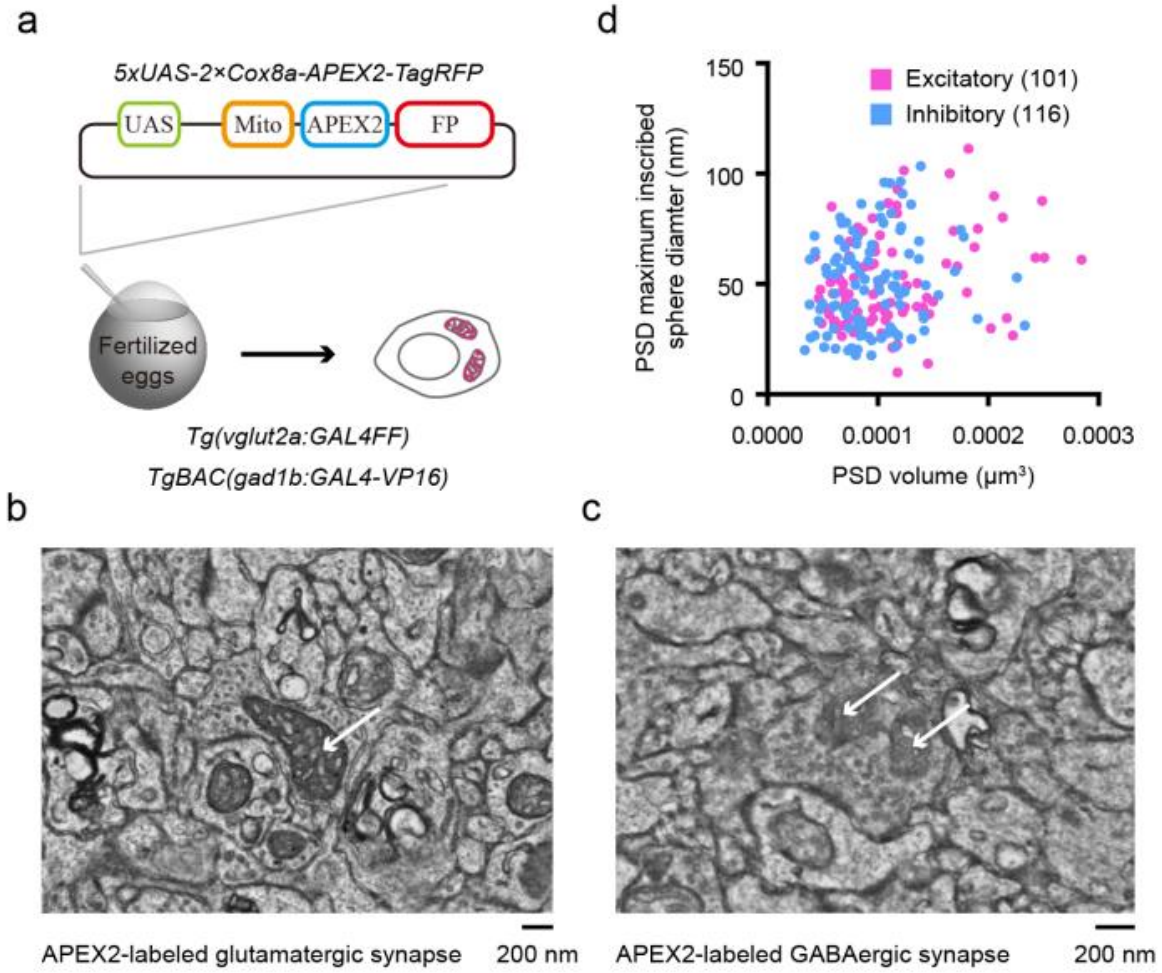


1162

1163

## Extended Data Fig.5

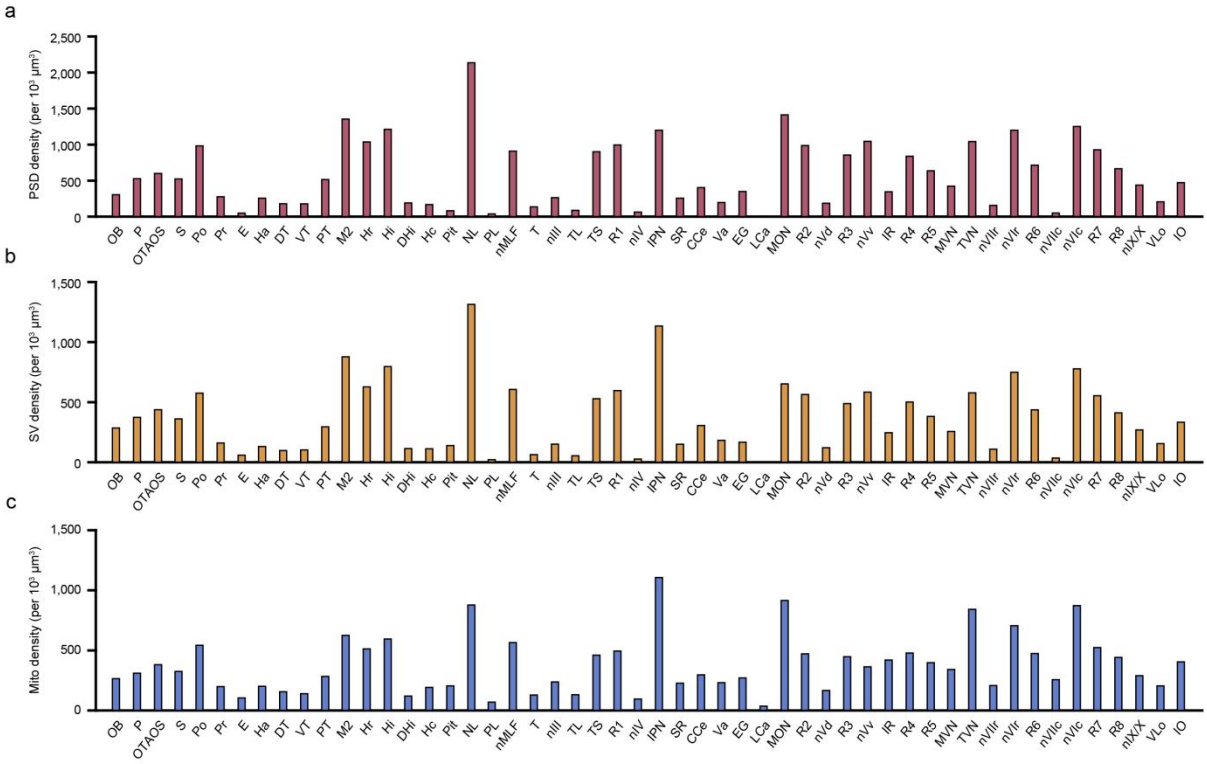

## Extended Data Fig.6

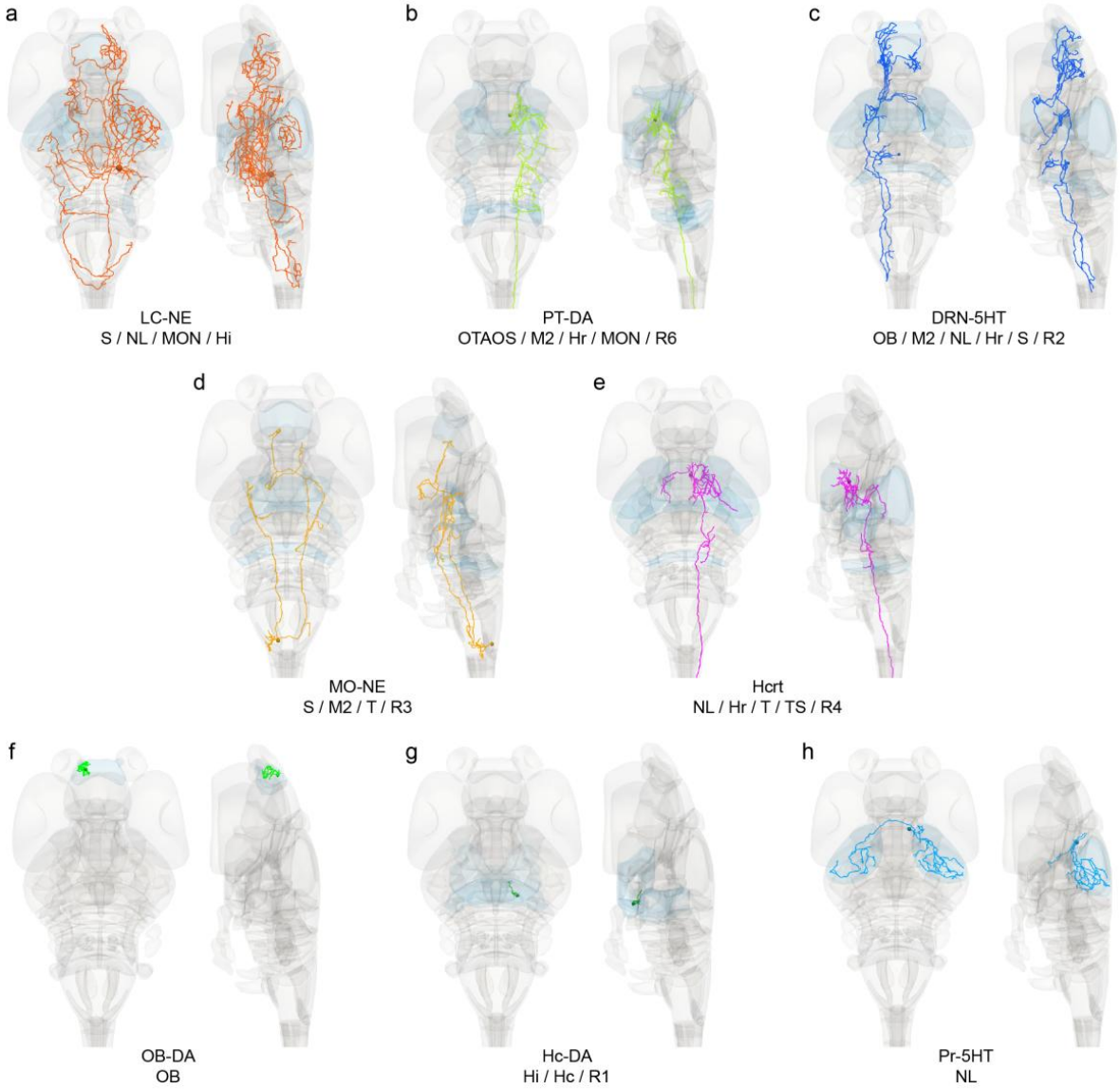

1170 **Extended Data Fig.7**

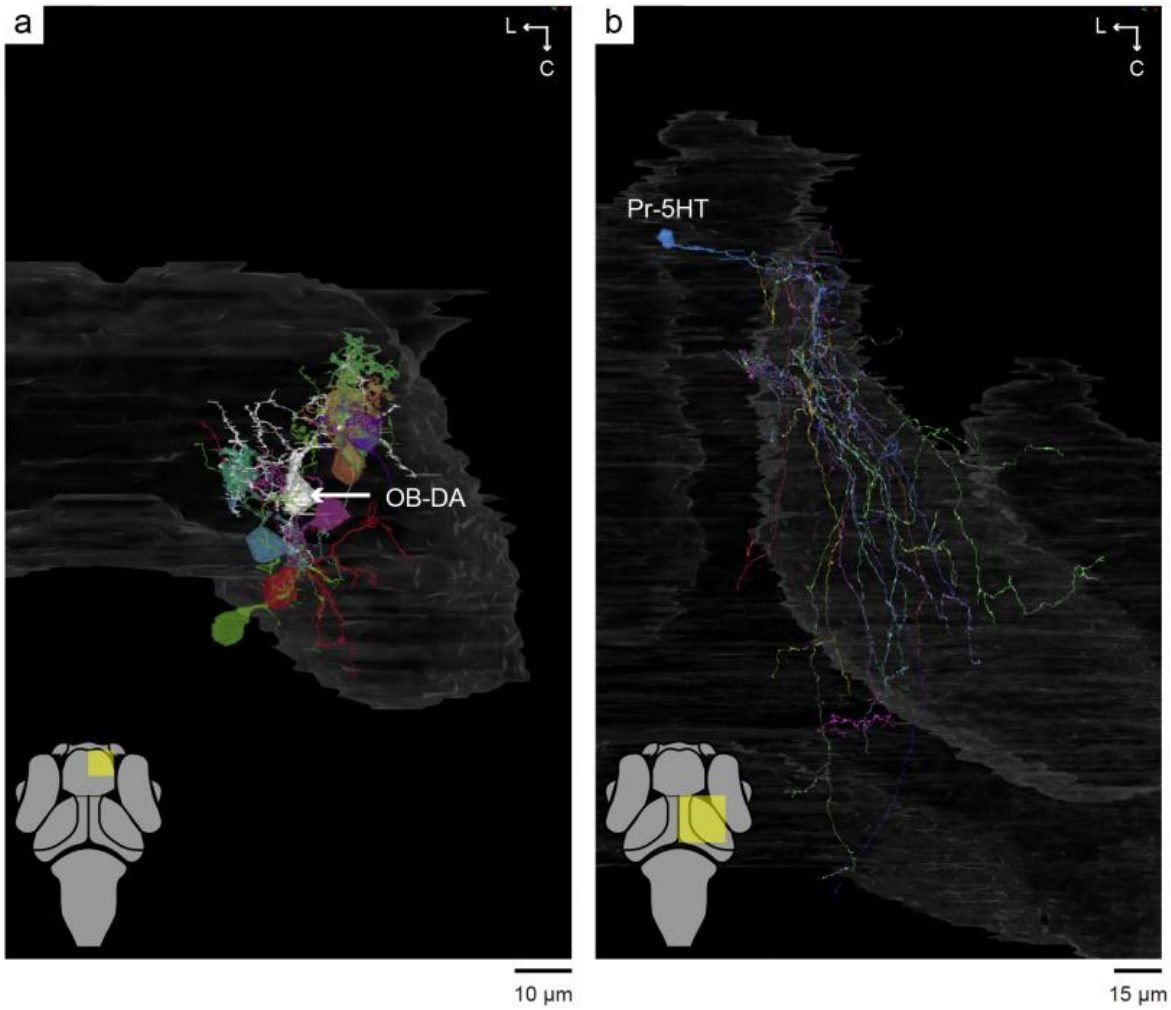


1171
1172
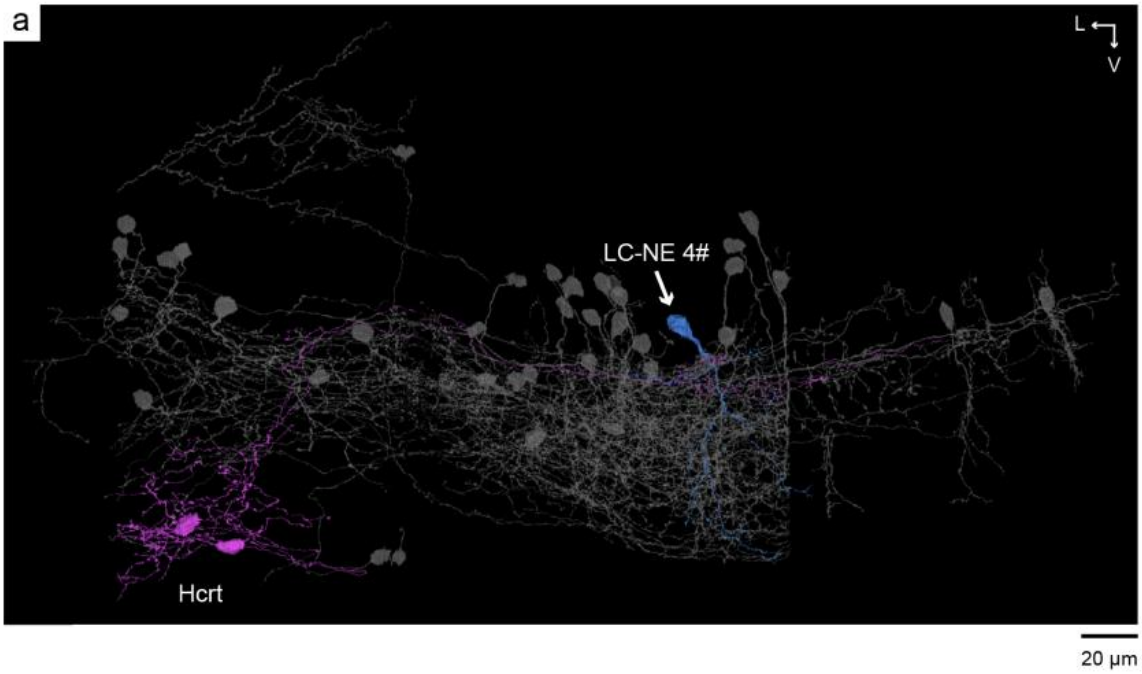
## Extended Data Fig.8